Monthly Notices
of the
ROYAL ASTRONOMICAL SOCIETY

MNRAS **502,** 2615–2629 (2021)
Advance Access publication 2021 January 22

doi:10.1093/mnras/stab170

Statistical modelling of the cosmological dispersion measure

Ryuichi Takahashi ,[1★] Kunihito Ioka ,[2] Asuka Mori[1] and Koki Funahashi[1]

[1] *Faculty of Science and Technology, Hirosaki University, 3 Bunkyo-cho, Hirosaki, Aomori 036-8561, Japan*
[2] *Yukawa Institute for Theoretical Physics, Kyoto University, Kyoto 606-8502, Japan*

Accepted 2021 January 18. Received 2020 December 15; in original form 2020 October 5

ABSTRACT

We have investigated the basic statistics of the cosmological dispersion measure (DM)—such as its mean, variance, probability distribution, angular power spectrum, and correlation function—using the state-of-the-art hydrodynamic simulations, IllustrisTNG300, for the fast radio burst cosmology. To model the DM statistics, we first measured the free-electron abundance and the power spectrum of its spatial fluctuations. The free-electron power spectrum turns out to be consistent with the dark matter power spectrum at large scales, but it is strongly damped at small scales ($\lesssim$ Mpc) owing to the stellar and active galactic nucleus feedback. The free-electron power spectrum is well modelled using a scale-dependent bias factor (the ratio of its fluctuation amplitude to that of the dark matter). We provide analytical fitting functions for the free-electron abundance and its bias factor. We next constructed mock sky maps of the DM by performing standard ray-tracing simulations with the TNG300 data. The DM statistics are calculated analytically from the fitting functions of the free-electron distribution, which agree well with the simulation results measured from the mock maps. We have also obtained the probability distribution of source redshift for a given DM, which helps in identifying the host galaxies of FRBs from the measured DMs. The angular two-point correlation function of the DM is described by a simple power law, $\xi(\theta) \approx 2400(\theta/\mathrm{deg})^{-1}\,\mathrm{pc}^2\,\mathrm{cm}^{-6}$, which we anticipate will be confirmed by future observations when thousands of FRBs are available.

Key words: methods: numerical – intergalactic medium – large-scale structure of Universe – radio continuum: transients.

1 INTRODUCTION

A fast radio burst (FRB) is a radio pulse (∼ms wide) coming from a cosmological distance (see reviews by Cordes & Chatterjee 2019 and Petroff, Hessels & Lorimer 2019). After the first detection (Lorimer et al. 2007), more than hundreds of FRBs have been reported to date (Petroff et al. 2016).[1] Ongoing and future surveys such as ASKAP,[2] CHIME,[3] UTMOST,[4] FAST,[5] STARE2 (Bochenek et al. 2020), and SKA[6] will detect thousands of events per year (e.g. Connor et al. 2016; Hashimoto et al. 2020). Many FRB-progenitor models have been proposed, but the origins of FRBs are still obscure (e.g. Popov & Postnov 2010; Kashiyama, Ioka & Mészáros 2013; Totani 2013; Cordes & Wasserman 2016; Murase, Kashiyama & Mészáros 2016; Kumar, Lu & Bhattacharya 2017; Metzger, Berger & Margalit 2017; Ioka 2020; Ioka & Zhang 2020; Levin, Beloborodov & Bransgrove 2020; Lyubarsky 2020).[7] More observations are needed to differentiate between them. From the frequency dependence of the arrival time from a FRB, the projected free-electron density along the line of light (i.e. the dispersion measure, DM) can be measured. Similarly, from the frequency dependence of the polarisation angle, the line-of-sight component of the magnetic field (i.e. the rotation measure) can also be measured. Because FRBs are extragalactic sources, these DMs and RMs directly map the cosmological free-electron distribution (Ioka 2003; Inoue 2004) and the cosmic magnetic fields (e.g. Akahori, Ryu & Gaensler 2016; Michilli et al. 2018).

The primordial abundance of baryons is currently measured to sub-per cent-level accuracy by the cosmic microwave background and big bang nucleosynthesis (BBN; Cooke, Pettini & Steidel 2018; Planck Collaboration VI 2020). However, in the late-time universe, the baryon abundance and its spatial distribution are still poorly constrained by observations (e.g. Fukugita & Peebles 2004; Shull, Smith & Danforth 2012). About one-third of the baryons are still missing (the so-called 'missing baryons'), although they are likely to be low-density ionized gas in the intergalactic medium (IGM). The cosmological DM is a powerful tool to probe for the missing baryons (Ioka 2003; Inoue 2004). Very recently, Macquart et al. (2020) measured the baryon density from five host-galaxy-identified FRBs. Their result is independent of, but consistent with, the *Planck* and BBN results. Keane et al. (2016) provided a similar constraint from a single event.

Because FRBs and their DMs have unique cosmological properties, many cosmological applications have been proposed. The DMs of far-distant FRBs are a unique probe of cosmological reionization (Ioka 2003; Inoue 2004; Caleb, Flynn & Stappers 2019; Dai & Xia 2020). Gravitational lensing of FRBs also enables searches for intervening compact objects that may constitute the dark matter (e.g. Zheng et al. 2014; Muñoz et al. 2016; Oguri 2019; Jow et al. 2020; Liao et al. 2020). If the host galaxy is identified, the redshift–DM relation can constrain the dark energy models (e.g. Gao, Li & Zhang

★ E-mail: takahasi@hirosaki-u.ac.jp
[1]FRB catalogue at http://frbcat.org.
[2]https://www.atnf.csiro.au/projects/askap/
[3]https://chime-experiment.ca/
[4]https://astronomy.swin.edu.au/research/utmost/
[5]https://fast.bao.ac.cn/
[6]https://www.skatelescope.org/
[7]https://frbtheorycat.org/index.php/Main_Page

2014; Zhou et al. 2014). The angular autocorrelation of the DM directly maps free-electron clustering (e.g. Masui & Sigurdson 2015; Shirasaki, Kashiyama & Yoshida 2017), and its large-scale signal may contain primordial non-Gaussianity (Reischke, Hagstotz & Lilow 2020). The cross-correlation of the DM and foreground galaxies provides the free-electron distribution around the galaxies (McQuinn 2014; Shirasaki et al. 2017; Madhavacheril et al. 2019), as well as helping to constrain the redshift distribution of the host galaxies (Rafiei-Ravandi, Smith & Masui 2019). The cross-correlation of the DM and the thermal Sunyaev–Zel'dovich signal (tSZ, Sunyaev & Zeldovich 1970) gives further information about ionized gas because the tSZ effect measures the projected electron pressure (Muñoz & Loeb 2018).

Theoretical studies of the DM statistics have been based on the analytical halo model or hydrodynamic simulations because these are able to explore the non-linear free-electron distribution. McQuinn (2014) calculated the DM statistics (variance and probability distribution) from the halo model (e.g. Cooray & Sheth 2002) for given model ingredients such as spatial halo clustering, halo mass function, and free-electron density profile in haloes. Madhavacheril et al. (2019) and Dai & Xia (2020) computed the angular power spectrum of the DM based on the halo model. Cosmological hydrodynamic simulations are the most reliable tools for investigating the free-electron distribution in the universe. Dolag et al. (2015) studied the DM probability distribution based on hydrodynamic simulations (the Magneticum Pathfinder; Dolag, Komatsu & Sunyaev 2016). Zhu, Feng & Zhang (2018) estimated the dispersion and scattering measures in the IGM using their cosmological hydrodynamic simulations. Pol et al. (2019) made a full-sky map of the DM using the MICE ONION simulation (Fosalba et al. 2008), and they computed the mean, variance, and probability distribution of the DM. That was a dark-matter-only (DMO) simulation, and they assumed that the free electrons exactly trace the dark matter. Shirasaki et al. (2017) performed a similar analysis using their own dark-matter simulation. Jaroszynski (2019) recently studied the cosmological DM (its mean, variance, and probability distribution) using a public hydrodynamic simulation, the original Illustris (Vogelsberger et al. 2014).

The previous simulation studies did not compare their measurements with analytical predictions of the DM statistics (such as its variance and power spectrum), where the analytical solutions are useful for future data analyses. Previous analytical studies on the DM statistics assumed that free electrons exactly trace the underlying dark matter (Masui & Sigurdson 2015; Shirasaki et al. 2017; Rafiei-Ravandi et al. 2019), although this assumption breaks down at small scales ($\lesssim 1$ Mpc), as shown in subsection 3.3. The main purpose of this work is to provide an analytical model for the DM statistics (such as its mean, variance, angular power spectrum, and correlation function). The analytical model is based on a standard two-point statistics. Because the DM statistics are fully determined by the free-electron statistics, we first measure the the free-electron distribution from the latest cosmological hydrodynamic simulations, IllustrisTNG, the successor to Illustris (e.g. Nelson et al. 2018). We use the largest box run from these TNG simulations (named TNG300, for which the side length of the cubic box is $L = 205\,h^{-1}$ Mpc $\simeq 300$ Mpc), which is suitable for cosmological studies. We measure the free-electron abundance and the power spectrum of its spatial fluctuations over a wide range of redshifts ($z = 0$–5) and scales ($\approx$0.1–200 h^{-1} Mpc) in TNG300. We then make fitting functions for them to model the free-electron distribution. The DM statistics are calculated analytically using these fitting functions. We next construct mock sky maps of the DM using the TNG300 data and measure the DM statistics from them to check the accuracy of the analytical model. The three spatial-resolution runs in TNG300 are used to check the numerical convergence of the results. The presented model is applicable, in principle, for other cross-correlations, such as DM–galaxy, DM–weak lensing, and DM–tSZ cross-correlations. As thousands of FRBs will be available in the relatively near future, we expect this kind of statistical study to be required. Throughout this paper, we mainly study the cosmological DM (i.e. excluding contributions from the Milky Way and host galaxies).

The rest of this paper is organized as follows: Section 2 introduces the theory of two-point DM statistics. Section 3 measures the free-electron abundance and its power spectrum in the TNG300 data and provides fitting functions for them. Section 4 describes a procedure for making mock sky maps of the DM. Section 5 presents our main results: comparisons between the simulation results measured from the mock maps and analytical predictions. Section 6 discusses the host-galaxy contribution and provides comparisons with other hydrodynamic simulations. Finally, Section 7 summarizes this work.

Throughout this paper, we adopt a cosmological model consistent with the *Planck* 2015 best-fitting flat ΛCDM model (Planck Collaboration XIII 2016): matter density $\Omega_{\rm m} = 1 - \Omega_\Lambda = 0.3089$, baryon density $\Omega_{\rm b} = 0.0486$, Hubble parameter $h = 0.6774$, spectral index $n_{\rm s} = 0.9667$, and amplitude of the matter density fluctuations on the scale of $8\,h^{-1}$ Mpc $\sigma_8 = 0.8159$. This model is the same as that adopted in the TNG simulations. All physical quantities (such as length, wavenumber, and number density) will be given in comoving units.

2 THEORY OF THE COSMOLOGICAL DISPERSION MEASURE

This section presents the theoretical basics of the cosmological DM: the mean and fluctuations (subsection 2.1) and the two-point statistics (subsection 2.2).

2.1 The mean and fluctuations

Three major components contribute to the observed DM: the Milky Way, the host galaxy, and the intervening cosmological medium. The Milky Way contribution can be inferred from the Galactic free-electron distribution, which is modelled by pulsar measurements (e.g. the NE2001 model: Cordes & Lazio 2002). The host-galaxy contribution decreases for more distant sources in proportion to $(1 + z_{\rm s})^{-1}$, where $z_{\rm s}$ is the source redshift, due to cosmological time dilation and the Doppler frequency shift (if its intrinsic property in the rest frame does not evolve with time, e.g. Zhou et al. 2014). In contrast, the cosmological contribution increases roughly in proportion to $z_{\rm s}$ (e.g. Ioka 2003), and it exceeds the host-galaxy contribution for $z_{\rm s} \gtrsim 0.3$. Therefore, throughout this paper, we mainly consider the cosmological contribution, and hereafter, DM refers to that alone. The host-galaxy contribution will be briefly discussed in subsection 6.1.

We consider an FRB at an angular position $\boldsymbol{\theta} = (\theta_1, \theta_2)$ on the sky and redshift $z_{\rm s}$, as shown in Fig. 1. The vector $\boldsymbol{r}$ points to the intervening gas at z, and its absolute value is the comoving distance

$$r(z) = \int_0^z \frac{c\,{\rm d}z'}{H(z')}, \tag{1}$$

where $H(z)$ is the Hubble expansion rate. Denoting the number density of free electrons at $\boldsymbol{r}$ and z by $n_{\rm e}(\boldsymbol{r}; z)$, the DM is obtained

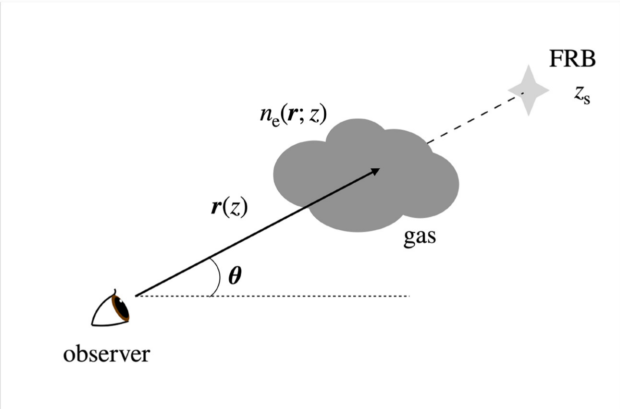

Figure 1. Schematic configuration of the observer, ionized gas and an FRB: $\boldsymbol{\theta}$ is the angular position of the FRB, $\boldsymbol{r}$ is a vector along the line of sight, and n_e is the number density of free electrons at $\boldsymbol{r}$.

by integrating n_e along the line of sight (e.g. Ioka 2003; Inoue 2004):

$$\mathrm{DM}(\boldsymbol{\theta}; z_s) = \int_0^{z_s} \frac{c\mathrm{d}z}{H(z)} n_e(\boldsymbol{r}; z)(1+z). \tag{2}$$

Note that the number density n_e is given in comoving units.

The number density n_e can be decomposed into its spatial mean $\bar{n}_e$ and fluctuations δ_e:

$$n_e(\boldsymbol{r}; z) = \bar{n}_e(z)\left[1 + \delta_e(\boldsymbol{r}; z)\right]. \tag{3}$$

The spatial average of the second term vanishes: $\langle \delta_e \rangle = 0$. As for the first term, the total number density of electrons (including both free electrons and those bound to atoms) in the universe is

$$\bar{n}_{e,\mathrm{total}} = \left(X_p + \frac{1}{2} Y_p\right) \frac{\bar{\rho}_b}{m_p}, \tag{4}$$

where $\bar{\rho}_b$ is the comoving cosmological baryon density and m_p is the proton mass (e.g. Deng & Zhang 2014). The quantities X_p and Y_p denote the primordial mass fractions of hydrogen and helium, respectively, and are set to $X_p = 1 - Y_p = 0.76$ to be consistent with TNG. We ignore the time evolution of $\bar{n}_{e,\mathrm{total}}$ due to stellar nucleosynthesis because it is negligibly small. Introducing the free-electron fraction at z, $f_e(z)$, the free-electron number density is written as

$$\bar{n}_e(z) = f_e(z)\, \bar{n}_{e,\mathrm{total}}, \tag{5}$$

where $f_e = 1$ corresponds to full ionization. After hydrogen and helium were fully ionized at $z \sim 3$, f_e is assumed to be close to unity. However, current observational constraints on f_e still have a large variation ($f_e \simeq 0.7$–1, e.g. Fukugita & Peebles 2004; Shull et al. 2012; McQuinn 2016; Walters et al. 2019; Li et al. 2020). Note that f_e in equation (5) includes all free electrons, both inside and outside of intervening galaxies. In other words, f_e is the spatial mean fraction averaged over all galaxies and the IGM. In this paper, we do not introduce the free-electron fraction in IGM, f_{IGM}. One reason is that f_{IGM} depends on the boundary between the galaxies and the IGM, and that boundary is ambiguous. Another reason is that some FRB signals may pass through an intervening galaxy; this probability may be low, but it gives a large DM. We will measure f_e from the TNG300 simulations in Section 3.

Similarly to n_e, the DM can be decomposed into two terms:

$$\mathrm{DM}(\boldsymbol{\theta}; z_s) = \overline{\mathrm{DM}}(z_s) + \delta\mathrm{DM}(\boldsymbol{\theta}; z_s). \tag{6}$$

The mean and fluctuations of the DM can be written from equations (2)–(5) in the forms

$$\overline{\mathrm{DM}}(z_s) = \int_0^{z_s} \frac{c\mathrm{d}z}{H(z)} W(z), \tag{7}$$

$$\delta\mathrm{DM}(\boldsymbol{\theta}; z_s) = \int_0^{z_s} \frac{c\mathrm{d}z}{H(z)} W(z) \delta_e(\boldsymbol{r}; z), \tag{8}$$

with a kernel

$$W(z) = \frac{\bar{\rho}_b}{m_p}\left(X_p + \frac{1}{2} Y_p\right) f_e(z)(1+z). \tag{9}$$

The mean baryon density is rewritten as $\bar{\rho}_b = \Omega_b\, \rho_{\mathrm{cr}} = 3H_0^2 \Omega_b/(8\pi G)$, where ρ_{cr} is the cosmological critical density.

2.2 The two-point statistics

This subsection discusses the angular correlation function and its Fourier transform (i.e. the power spectrum) of the DM fluctuations. Previously, several authors have studied the angular power spectrum of the DM (e.g. Masui & Sigurdson 2015; Shirasaki et al. 2017; Madhavacheril et al. 2019; Dai & Xia 2020). Here, we simply summarize their results.[8]

The angular correlation function of the DM between $\boldsymbol{\theta}_1$ and $\boldsymbol{\theta}_2$ at the same source redshift z_s is defined as

$$\xi(\theta_{12}; z_s) \equiv \langle \delta\mathrm{DM}(\boldsymbol{\theta}_1; z_s)\, \delta\mathrm{DM}(\boldsymbol{\theta}_2; z_s) \rangle. \tag{10}$$

Because of the isotropy of the universe, the correlation function is a function of the separation $\theta_{12} = |\boldsymbol{\theta}_1 - \boldsymbol{\theta}_2|$. Throughout this paper, we assume $|\theta_{12}| \ll 1$, i.e. the flat-sky approximation is valid. From equations (8) and (10), under the Limber and the flat-sky approximations, the correlation function reduces to

$$\xi(\theta_{12}; z_s) = \frac{1}{2\pi} \int_0^{z_s} \frac{c\mathrm{d}z}{H(z)} W^2(z) \int_0^{\infty} \mathrm{d}k k\, P_e(k; z) J_0\left(\theta_{12} k r(z)\right), \tag{11}$$

where J_0 is the zeroth order Bessel function and k is the wavenumber of the density fluctuations. The power spectrum of the free-electron fluctuations is defined as

$$P_e(k; z)\, (2\pi)^3\, \delta_D^3(\boldsymbol{k} + \boldsymbol{k}') \equiv \langle \tilde{\delta}_e(\boldsymbol{k}; z) \tilde{\delta}_e(\boldsymbol{k}'; z) \rangle, \tag{12}$$

where $\tilde{\delta}_e(\boldsymbol{k}; z)$ is the Fourier transform of $\delta_e(\boldsymbol{r}; z)$ and δ_D is the Dirac delta function.

The Fourier transform of the DM fluctuations is given by

$$\widetilde{\delta\mathrm{DM}}(\boldsymbol{\ell}; z_s) = \int \mathrm{d}^2\boldsymbol{\theta}\, \delta\mathrm{DM}(\boldsymbol{\theta}; z_s)\, \mathrm{e}^{-\mathrm{i}\boldsymbol{\ell}\boldsymbol{\theta}}, \tag{13}$$

where $\boldsymbol{\ell} = (\ell_1, \ell_2)$ is the two-dimensional vector of multipole moments. Similarly to $P_e(k; z)$, the angular power spectrum of the DM is defined as

$$C_\ell(z_s)\, (2\pi)^2\, \delta_D^2(\boldsymbol{\ell} + \boldsymbol{\ell}') \equiv \langle \widetilde{\delta\mathrm{DM}}(\boldsymbol{\ell}; z_s) \widetilde{\delta\mathrm{DM}}(\boldsymbol{\ell}'; z_s) \rangle. \tag{14}$$

From the above equations (10)–(14), the angular power spectrum is obtained as

$$C_\ell(z_s) = \int \mathrm{d}^2\boldsymbol{\theta}\, \xi(\theta; z_s)\, \mathrm{e}^{-\mathrm{i}\boldsymbol{\ell}\boldsymbol{\theta}},$$
$$= \int_0^{z_s} \frac{c\mathrm{d}z}{H(z)} \frac{W^2(z)}{r^2(z)} P_e\left(k = \frac{\ell}{r(z)}; z\right). \tag{15}$$

This equation relates the 3D power spectrum of the free electrons to the 2D power spectrum of the DM.

[8] A detailed discussion of the two-point statistics of projected random fields is found in, e.g. section 2.4 of Bartelmann & Schneider (2001) and section 9.1 of Dodelson (2003).

Table 1. Summary of the TNG300 simulations used in this paper: the numbers of baryon and dark-matter particles ($N_{\rm baryon}$, $N_{\rm dark}$), the average masses of baryon and dark-matter particles ($m_{\rm baryon}$, $m_{\rm dark}$), the minimum gravitational softening length of the gas cells ($\epsilon_{\rm gas,\,min}$), and the mean size of the gas cells ($r_{\rm gas} \equiv L/N_{\rm baryon}^{1/3}$). The upper three runs follow both the gravitational evolution and astrophysical processes, while the bottom one follows only the former. The side length of the simulation box is $L = 205\,h^{-1}$ Mpc in all runs.

	$N_{\rm baryon}$	$N_{\rm dark}$	$m_{\rm baryon}(h^{-1}{\rm M}_\odot)$	$m_{\rm dark}(h^{-1}{\rm M}_\odot)$	$\epsilon_{\rm gas,\,min}(h^{-1}{\rm kpc})$	$r_{\rm gas}(h^{-1}$ kpc)
TNG300-1	2500^3	2500^3	7.4×10^6	4.0×10^7	0.25	82
TNG300-2	1250^3	1250^3	6.0×10^7	3.2×10^8	0.5	164
TNG300-3	625^3	625^3	4.8×10^8	2.5×10^9	1.0	328
TNG300-1-Dark	–	2500^3	–	4.7×10^7	–	–

Table 2. Output redshift z, comoving distance $r(z)$, and snapshot number in the TNG data set.

z	$r(z)\,(h^{-1}$Mpc)	Snapshot
0	0	99
0.1	293	91
0.2	571	84
0.3	834	78
0.4	1083	72
0.5	1318	67
0.7	1747	59
1	2301	50
1.5	3034	40
2	3599	33
3	4411	25
4	4973	21
5	5390	17
6	5716	13
7	5978	11
8	6196	8

The variance of the DM is simply obtained by setting $\boldsymbol{\theta}_1 = \boldsymbol{\theta}_2$ in equations (10) and (11):

$$\sigma^2_{\rm DM}(z_{\rm s}) \equiv \langle [\delta {\rm DM}(\boldsymbol{\theta}; z_{\rm s})]^2 \rangle,$$
$$= \frac{1}{2\pi} \int_0^{z_{\rm s}} \frac{c{\rm d}z}{H(z)} W^2(z) \int_0^\infty {\rm d}k k\, P_{\rm e}(k; z). \quad (16)$$

This is consistent with the analytical result in McQuinn (2014, their section 2). Theoretical models of the ionized fraction $f_{\rm e}(z)$ and the power spectrum $P_{\rm e}(k; z)$ are required to compute the above two-point statistics. We will calibrate these functions using TNG300 in the next section.

3 CALIBRATION WITH TNG300

This section briefly introduces the TNG simulations (subsection 3.1) and then measures the free-electron fraction $f_{\rm e}(z)$ (subsection 3.2) and the power spectrum $P_{\rm e}(k; z)$ (subsection 3.3).

3.1 The TNG simulations

We investigate the spatial distribution of free electrons in the universe using the TNG data set[9] (Marinacci et al. 2018; Naiman et al. 2018; Nelson et al. 2018; Springel et al. 2018; Pillepich et al. 2018b). The simulations follow the gravitational clustering of matter (dark matter and baryons) as well as astrophysical processes such as star and galaxy formation, gas cooling, and stellar and active galactic nucleus (AGN) feedback. The gravitational evolution and magneto-hydrodynamic processes were computed with the moving-mesh code AREPO (Springel 2010). The simulations incorporate astrophysical processes in a subgrid model, thereby enabling them to follow the processes of galaxy formation and evolution. The TNG project produced three sets of simulations in different-sized cubic boxes, with three mass resolutions for each box size. Here, we used the largest box (referred to as TNG300), with side length $L = 205\,h^{-1}$ Mpc ($\simeq 300$ Mpc) because our interest is the large-scale distribution of free electrons. To check the numerical convergence, we used the three resolutions from high to low (referred to as TNG300-1 to -3, respectively). This box contains the same number of dark matter and baryon particles. The number of particles and the mass resolution are listed in Table 1. The TNG team also performed DMO runs, in which the number of dark-matter particles was the same as in TNG300. In this case, the N-body particles represent both components (baryons and dark matter), but the simulations follow the gravitational evolution only. Such simulations help to see the impact of dark matter on the free-electron clustering. Here, we used the highest resolution run (named TNG300-1-Dark). The TNG team have released the simulation data at 20 redshifts in the range $z =$ 0–12 (named 'full' snapshots). In this paper, we used all the data sets up to $z = 8$, as listed in Table 2. The first column is the redshift z, the second is the comoving distance to z and the third refers to the TNG snapshot number.

Table 3. Mass fractions of gas, stars, and supermassive black holes to the total baryons measured in TNG300-1. The values are given in percentages (i.e. $f_{\rm gas} + f_{\rm star} + f_{\rm bh} = 100\,\%$). The gas is further decomposed into neutral and ionized hydrogen (H_0 and H^+) and helium (He), which satisfy $f_{\rm gas} \simeq f_{\rm H_0} + f_{\rm H^+} + f_{\rm He}$.

z	$f_{\rm gas}$	$f_{\rm H_0}$	$f_{\rm H^+}$	$f_{\rm He}$	$f_{\rm star}$	$f_{\rm bh}$
0	96.8	1.4	71.9	23.3	3.2	0.02
1	97.7	0.9	73.2	23.5	2.3	0.01
3	99.3	0.9	74.6	23.8	0.7	5×10^{-3}
5	99.8	1.3	74.5	24.0	0.2	1×10^{-3}
6	99.9	74.0	1.9	24.0	0.1	$<10^{-3}$
7	100.0	75.0	1.0	24.0	0.06	$<10^{-3}$
8	100.0	75.5	0.4	24.0	0.03	$<10^{-3}$

Each baryon particle has one of three forms: gas, star, or supermassive black hole. Free electrons are contained only in the gas particles. At the initial redshift ($z = 127$), all the baryon particles are gas. As time evolves, the gas falls into the haloes, and star formation begins in high-density regions (Pillepich et al. 2018a). Some gas particles then convert to stars or black holes. However, even at $z = 0$, most of the baryon particles are still gas (the gas mass fraction is > 96 per cent). The time evolution of each mass fraction measured in TNG300-1 is summarized in Table 3. The mass fraction is obtained from the total

[9]The simulation data are available at http://www.tng-project.org.

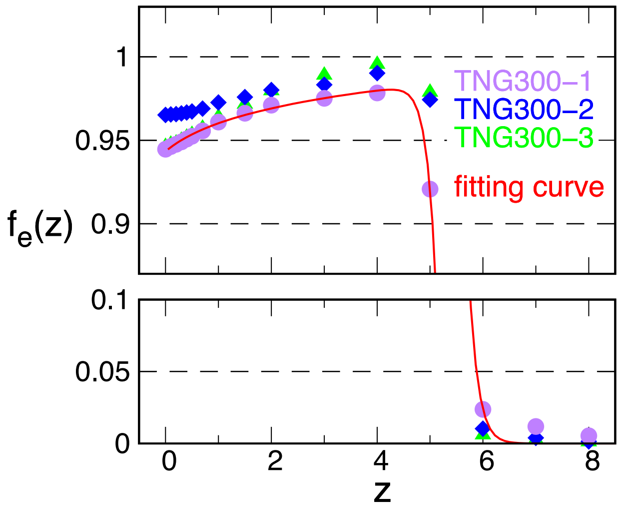

Figure 2. Time evolution of the free-electron fraction measured in TNG300. The purple, blue, and green symbols represent the results from TNG300-1, -2, and -3 (from high- to low-resolution runs), respectively. The red curve is the fit to TNG300-1 given in equation (17).

mass of each component in the box divided by the total baryonic mass ($=\bar{\rho}_b L^3$). The TNG team followed the time evolution of the atomic abundances of H, He, and seven other species (C, N, O, Ne, Mg, Si, and Fe). The public data contains the atomic abundance in each gas particle. For hydrogen, the data includes neutral (H_0) and ionized (H^+) fractions. In Table 3, the gas mass fraction (f_{gas}) is further decomposed into neutral and ionized hydrogen (f_{H_0} and f_{H^+}) and helium (f_{He}), where f_{He} includes both neutral and ionized states. The mass fraction of elements heavier than He is negligible. The hydrogen is ionized abruptly at the epoch of cosmic reionization (between $z =$ 5 and 6). We comment that the mass fraction of stars (f_{star}) reaches 3.2 per cent at $z = 0$, which is slightly smaller than the observed values $f_{star} = 6.0 \pm 1.3$ per cent (Fukugita & Peebles 2004) and 7 ± 2 per cent (Shull et al. 2012; Nicastro et al. 2018). Therefore, the gas fraction f_{gas} and the resulting free-electron fraction f_e in TNG300-1 may be overestimated by approximately a few per cent.

Previous work (Jaroszynski 2019) on the DM used the lowest resolution run of Illustris: the side length of the box is $75\,h^{-1}$ Mpc, and it contains 2×455^3 baryon and dark-matter particles. Therefore, TNG300 has better mass resolution and a larger simulation volume. Their work did not check the numerical convergence among the different resolutions. Illustris is known to predict AGN feedback that is too strong (e.g. Chisari et al. 2019), which may affect the free-electron distribution in the haloes.

3.2 Free-electron abundance

The TNG team also provided the abundance of free electrons in each gas particle, which is the total free-electron abundance for all atoms (not only for hydrogen). By summing up all the gas particles in each snapshot, we obtained the number density of free electrons and its fraction, $\bar{n}_e(z)$ and $f_e(z)$, as defined in equation (5). Here, we measured $f_e(z)$ at the 16 redshifts in the range $z = 0$–8 listed in Table 2. The result is plotted in Fig. 2. At high $z\,(\gtrsim 6)$, the gas is still neutral (i.e. $f_e \simeq 0$). The fraction f_e rises abruptly at the epoch of hydrogen reionization ($z \sim 6$) and increases further at the epoch of helium reionization ($z \sim 4$). At relatively low $z\,(\lesssim 3)$, f_e decreases slightly because some fraction of the electrons becomes confined in stars and black holes (see Table 3). A small fraction of the electrons is in neutral hydrogen (H I and H_2) in galaxies ($f_{H_0} \sim 1$ per cent in Table 3; the cosmological H I distribution was recently studied using hydrodynamic simulations in, e.g. Villaescusa-Navarro et al. 2018; Ando et al. 2019).

The TNG300-1 result can be fitted by

$$f_e(z) = a\,(z+b)^{0.02}\,[1 - \tanh\{c(z-z_0)\}]\,, \tag{17}$$

with $a = 0.475$, $b = 0.703$, $c = 3.19$, and $z_0 = 5.42$. Here, z_0 corresponds to the epoch of hydrogen reionization. For $z \gg z_0$, f_e approaches zero. On the other hand, for $z \to 0, f_e \to 2a \simeq 0.95$. This fit agrees with the TNG300-1 results to within a deviation $\Delta f_e =$ 0.012 in the range $z = 0$–8. There are few per cent deviations among the different resolution runs, and thus, this fit has the same level of error. Note that our f_e corresponds to the quantity f_{ion} defined in a previous work (Jaroszynski 2019). Their result is slightly higher than ours, but the difference is very small ($f_{ion} \simeq 0.98$–0.99 in the range $z = 0$–4, see their table 2).

We comment that the TNG simulations followed the ionizing state of IGM using the time-dependent spatially uniform UV background radiation (instead of solving radiative transfer equations) with corrections for self-shielding in dense gas. This ionizing background started at $z = 6$, and thus the results of f_e at $z \geq 6$ should be considered with caution (see section 5.2 of Nelson et al. 2019; section 2.1.2 of Pillepich et al. 2018a). In the following, the simulation data up to $z = 5$ will be used.

3.3 Free-electron power spectrum

We next measured the power spectrum of free electrons in TNG300 following the standard procedure (see e.g. Springel et al. 2018, their section 2.2). The TNG team provided the mass of free electrons in each gas particle. To measure the density contrast, we assigned the free-electron mass to 1024^3 regular grid cells in the box using the cloud-in-cell interpolation with the interlacing scheme (e.g. Jing 2005; Sefusatti et al. 2016). The Fourier transform of the density field $\tilde{\delta}_e(\boldsymbol{k})$ was then obtained with fast Fourier transform (FFT).[10] To explore smaller scales, we also employed the folding method (Jenkins et al. 1998), which folds the particle positions $\boldsymbol{x}$ into a smaller box of side length $L/10$ by replacing $\boldsymbol{x}$ with $\boldsymbol{x}\%(L/10)$ (where $a\%b$ denotes the reminder of a/b). This procedure effectively increases the spatial resolution by 10 times. The minimum and maximum wavenumbers in the 1024^3 cells are $k_{min} = 2\pi/L = 0.025\,h\,\mathrm{Mpc}^{-1}$ (where $L = 205\,h^{-1}$ Mpc) and $k_{max} = 512\,k_{min} = 12.9\,h\,\mathrm{Mpc}^{-1}$, respectively. The folding scheme enlarges k_{max} by 10 times. The power spectrum is reliable up to the particle Nyquist wavenumber, which is determined by the mean separation of the gas particles r_{gas} in Table 1: $k_{Nyq} = \pi/r_{gas}$. The values of k_{Nyq} are 38.3 (19.1 and 9.6) $h\,\mathrm{Mpc}^{-1}$ for TNG300-1 (-2 and -3).

The power spectrum is measured as

$$P_e(k) = \frac{1}{N_{mode}} \sum_{|\boldsymbol{k}'| \in k} \left|\tilde{\delta}_e(\boldsymbol{k}')\right|^2, \tag{18}$$

where the summation is performed in the spherical shell $k - \Delta k/2 < |\boldsymbol{k}'| < k + \Delta k/2$ and N_{mode} is the number of Fourier modes in the shell with bin-width ($\Delta\log_{10}k = 0.1$). The spectrum $P_e(k)$ in

[10] Fast Fourier Transform in the West (FFTW) at http://www.fftw.org.

equation (18) contains the shot noise contribution

$$P_{\rm e,shot} = \frac{L^3}{N_{\rm eff}}, \tag{19}$$

where $N_{\rm eff}$ is the effective number of gas particles in the box. Denoting $m_{\rm i}$ as the free-electron mass of the i-th gas particle, we have $N_{\rm eff} = (\sum_{\rm i} m_{\rm i})^2/(\sum_{\rm i} m_{\rm i}^2)$. If all gas particles have equal mass, then $N_{\rm eff} = N_{\rm gas}$ (where $N_{\rm gas}$ is the number of gas particles). The shot noise was subtracted from the measured $P_{\rm e}(k)$. Here, we measured $P_{\rm e}(k)$ up to $z = 5$ because $P_{\rm e}(k)$ is noisy for $z \geq 6$ owing to the low free-electron abundance.

We also measured the matter power spectrum $P_{\rm DMO}(k)$ in the DMO run (TNG300-1-Dark in Table 1). This spectrum $P_{\rm DMO}(k)$ can be used to clarify the difference in clustering between free electrons and dark matter.

Fig. 3 plots the measured power spectra at several redshifts ($z =$ 0–3). The purple, blue, and green symbols are $P_{\rm e}(k)$, while the grey circles are $P_{\rm DMO}(k)$. The dotted lines denote the shot-noise contribution. The vertical axis is $k^2P_{\rm e}(k)$, which represents the contribution to the DM variance per ln$k$ from equation (16). The figure shows that density fluctuations at $k = 1$–$10\,h\,{\rm Mpc}^{-1}$ (corresponding to a scale of $2\pi/k \simeq 1\,{\rm Mpc}$) contribute most to the DM variance. The shot noise is negligibly small around this peak. The spectrum $P_{\rm e}(k)$ agrees with $P_{\rm DMO}(k)$ at large scales ($k < 1\,h\,{\rm Mpc}^{-1}$) but is strongly suppressed at intermediate and small scales ($k \gtrsim 1\,h\,{\rm Mpc}^{-1}$). Springel et al. (2018) previously measured the power spectrum of the gas in the TNG simulations and gave a physical explanation for this suppression: the stellar and AGN feedback expels gas from the haloes and suppresses the gas clustering, especially at low z, but gas cooling enhances clustering at very small scales, $k > 10\,h\,{\rm Mpc}^{-1}$. In fact, $k^2P_{\rm e}(k)$ rises slightly for $k > 10\,h\,{\rm Mpc}^{-1}$, especially for the higher resolution run. The results for $P_{\rm e}(k)$ at small scales ($k \gtrsim 10\,h\,{\rm Mpc}^{-1}$) do not converge among the different-resolution runs owing to the lack of spatial resolution. The orange-dashed curves are Halofit results from a fitting formula for non-linear $P_{\rm DMO}(k)$ (Smith et al. 2003; Takahashi et al. 2012). These curves agree with the DMO simulation results very well.

To model $P_{\rm e}(k; z)$, we introduce the bias factor $b_{\rm e}(k; z)$ defined by

$$b_{\rm e}^2(k;z) \equiv \frac{P_{\rm e}(k;z)}{P_{\rm DMO}(k;z)}. \tag{20}$$

Fig. 4 plots the measured bias. The bias approaches unity in the small-k limit, but it is suppressed at large k ($\gtrsim 1\,h\,{\rm Mpc}^{-1}$). At the largest scales (i.e. the smallest k), the bias is very close to unity, although it is slightly smaller than unity (by approximately a few per cent), especially at high z.[11] This is because the baryon-density fluctuations gradually catch up to the dark-matter fluctuations after the epoch of decoupling (at $z \simeq 1100$). The red curves are our fits to TNG300-1, where the bias is calibrated at 10 redshifts in the range $z = 0$–5 ($z =$ 0, 0.2, 0.4, 0.7, 1, 1.5, 2, 3, 4, and 5). The range of k included in the fit is determined such that the TNG300-1 and -2 results agree to within 20 per cent. The bias factor is fitted by the function

$$b_{\rm e}^2(k;z) = \frac{b_*^2(z)}{1 + \{k/k_*(z)\}^{\gamma(z)}}, \tag{21}$$

with

$$b_*^2(z) = 0.971 - 0.013\,z,$$
$$\gamma(z) = 1.91 - 0.59\,z + 0.10\,z^2,$$
$$k_*(z) = 4.36 - 3.24\,z + 3.10\,z^2 - 0.42\,z^3,$$

where k_* has units of $h\,{\rm Mpc}^{-1}$. This function agrees with the simulation results for $P_{\rm e}(k;z)/P_{\rm DMO}(k;z)$ to within 3.5 (10.8) per cent for $k < 2\,(10)\,h{\rm Mpc}^{-1}$ in the range $z = 0$–5.

The user can compute $P_{\rm e}(k)$ from the bias factor (21) and the $P_{\rm DMO}(k)$ model. Accurate fitting formulas for non-linear $P_{\rm DMO}(k)$ have been presented, such as Halofit (Smith et al. 2003; Takahashi et al. 2012), HMcode (Mead et al. 2015), and the Mira-Titan emulator (Lawrence et al. 2017). These formulas agree with the latest dark-matter simulations to within 5 per cent up to $k = 10\,h\,{\rm Mpc}^{-1}$ (e.g. Smith & Angulo 2019, their fig. 6). Halofit and HMcode are implemented in public codes such as CAMB[12] and CLASS.[13]

4 MAKING MOCK SKY MAPS OF THE DM

This section describes our procedure for making mock maps of the DM. We placed the simulation boxes along the line-of-sight direction using periodic boundary conditions, as shown in Fig. 5. The observer is placed at a corner of the box at $z = 0$. The field of view was set to be a square of $6 \times 6\,{\rm deg}^2$. To avoid repeating the same structure along the line of sight, we tilted the main axis (denoted by the dotted line) of the line of sight by 5° from the box axis. The lower z box in Table 2 was placed closer to the observer. For a given comoving distance r, we used the box nearest to r. For instance, from Table 2, the lowest z box (at $z = 0$) was used for $r/(h^{-1}\,{\rm Mpc}) \leq 293/2$, the second-lowest box (at $z = 0.1$) was used for $293/2 < r/(h^{-1}\,{\rm Mpc}) \leq (293 + 571)/2$ and so on. Note that, due to the periodicity of the box, for $r > 205\,h^{-1}\,{\rm Mpc}/(6\,{\rm deg}) \approx 2.0\,h^{-1}\,{\rm Gpc}$, the same structure may appear more than once in the field of view.

Free electrons are included in the gas particles. For each gas particle, the TNG team provided the spatial position, gas mass $m_{\rm gas}$, density $\rho_{\rm gas}$, and free-electron number density $n_{\rm e}^{\rm gas}$. We assume that each gas particle is described by a sphere of constant density with the radius $r_{\rm gas}$ determined via $m_{\rm gas} = (4\pi r_{\rm gas}^3/3)\rho_{\rm gas}$.

The DM is rewritten from equation (2) as

$${\rm DM}(\boldsymbol{\theta}; z_{\rm s}) = \int_0^{r_{\rm s}} {\rm d}r\, n_{\rm e}(\boldsymbol{r}; z)\,(1 + z(r))\,, \tag{22}$$

where $r_{\rm s} \equiv r(z_{\rm s})$ is the comoving distance to the source, and $\boldsymbol{\theta}$ denotes the angular position in the field of view, i.e. $\boldsymbol{\theta} = (\theta_1, \theta_2)$ with $|\theta_{1,2}| \leq 3$ deg. Light rays are emitted from the observer and propagate along straight lines in the field. The DM is computed by summing the contributions from all gas particles intersecting the light-ray path:

$${\rm DM}(\boldsymbol{\theta}; z_{\rm s}) = \sum_{\rm i} n_{\rm e,i}^{\rm 2D}(b_{\rm i})(1 + z_{\rm i}), \tag{23}$$

where $n_{\rm e,i}^{\rm 2D}$ is the free-electron column density of the i-th gas particle and $b_{\rm i}$ is the impact parameter (i.e. the minimum separation between the ray path and the position of the i-th particle). The redshift $z_{\rm i}$ is calculated from the comoving distance using equation (1). Assuming that the i-th gas particle has a constant density $n_{\rm e,i}^{\rm gas}$ and radius $r_{\rm gas,\,i}$, its column density profile is given by

$$n_{\rm e,i}^{\rm 2D}(b_{\rm i}) = 2\,n_{\rm e,i}^{\rm gas}\sqrt{r_{\rm gas,i}^2 - b_{\rm i}^2}\,, \tag{24}$$

[11] Shaw, Rudd & Nagai (2012) previously measured $b_{\rm e}^2(k)$ from their hydrodynamic simulations. Their result is somewhat smaller than ours in the low-k limit: $b_{\rm e}^2(k) = 0.6$–1 and varies with z (see the right-hand panel of their fig. 2). However, according to the cosmological perturbation theory of mixed components (baryons and dark matter), the baryon-fluctuation amplitude is only slightly smaller (< 4 per cent) than the dark matter one for $k \leq 0.1\,h\,{\rm Mpc}^{-1}$ and $z \leq 3$ (e.g. Somogyi & Smith 2010, their fig. 1).

[12] https://camb.info/

[13] http://class-code.net/

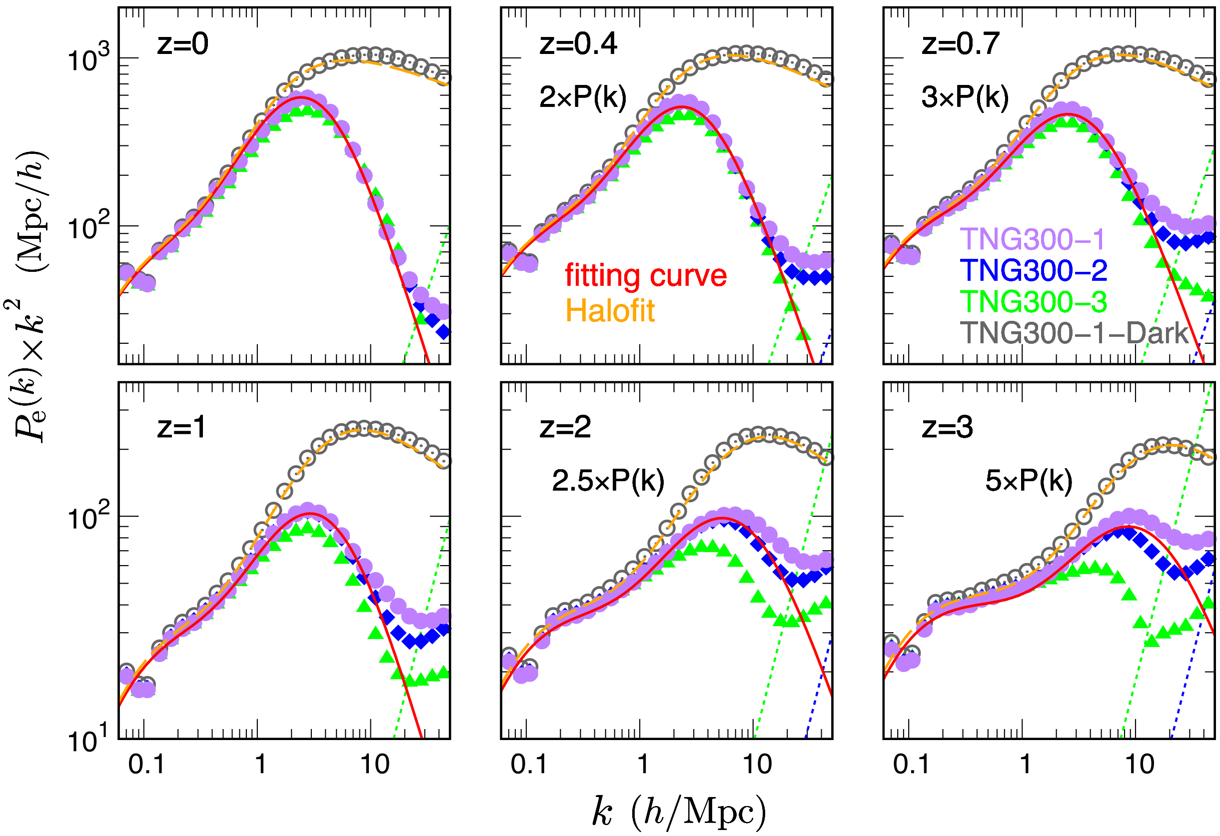

Figure 3. Free-electron power spectra $P_e(k)$ at $z = 0$–3 measured from TNG300. The purple, blue, and green symbols are the results from TNG300-1, -2 and -3, respectively. The grey circles are the matter power spectrum $P_{\rm DMO}(k)$ in the dark-matter-only run (TNG300-1-Dark). The orange-dashed curves are Halofit results for non-linear $P_{\rm DMO}(k)$ (Takahashi et al. 2012). The solid red curves are our fits: the free-electron bias factor, $b_e^2(k)$ in equation (21), times the Halofit. The green- and blue-dotted lines are the shot noise for TNG300-3 and -2, respectively. In the middle and right-hand panels, the results are multiplied by factors of 2–5 (as indicated in each panel) to make the presentation clearer.

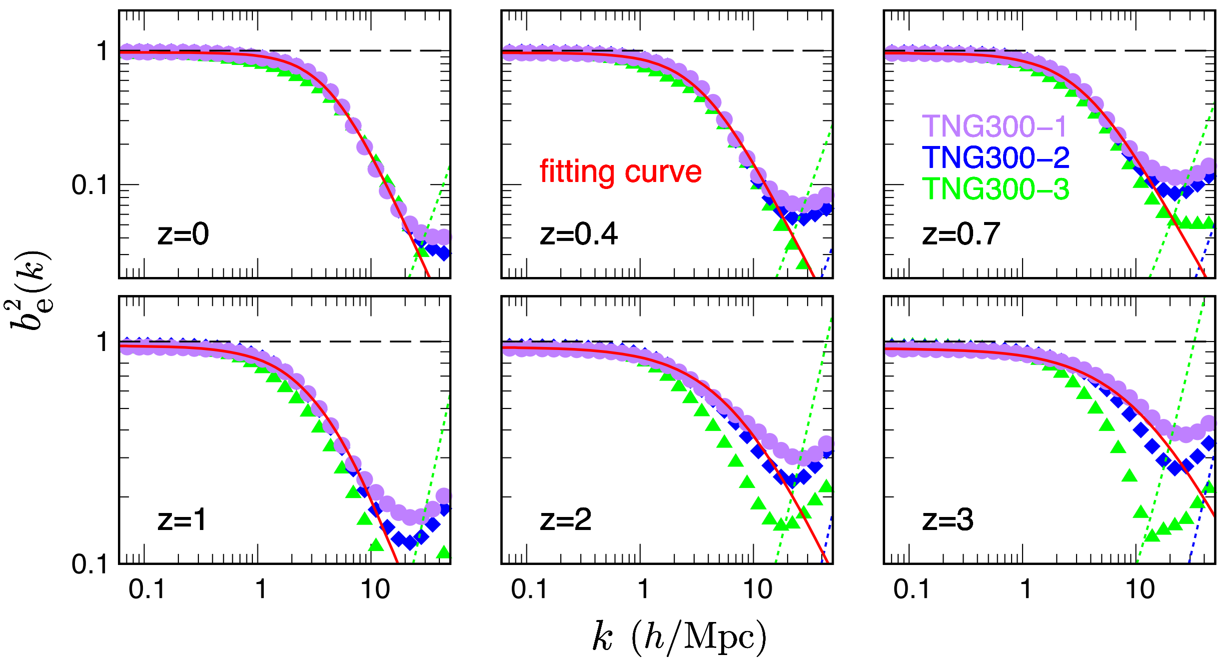

Figure 4. Similar to Fig. 3, but showing the free-electron bias factor defined as $b_e^2(k) = P_e(k)/P_{\rm DMO}(k)$. The red curves are the fits to TNG300-1 given by equation (21). The dotted lines denote the shot noise, and the horizontal dashed lines are $b_e = 1$.

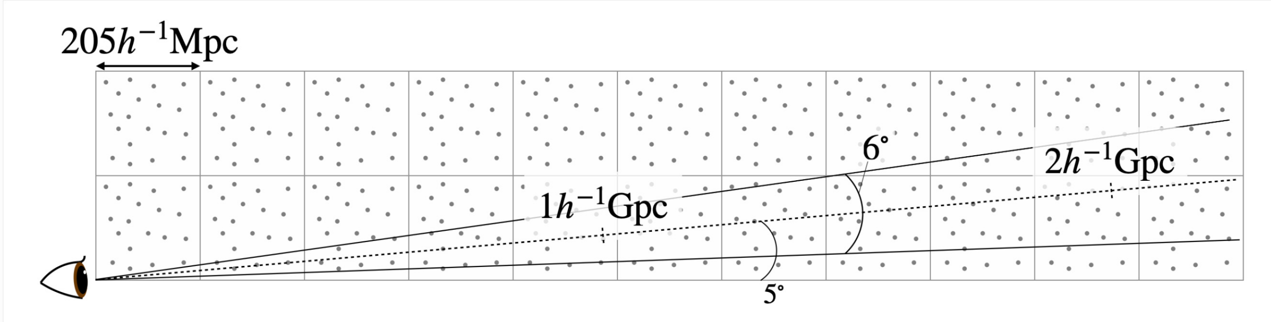

Figure 5. Schematic picture of our ray-tracing simulation setting. The grey squares represent the TNG300 simulation boxes with periodic boundary conditions. The field of view is $6 \times 6\,\mathrm{deg}^2$.

for $b_i < r_{\mathrm{gas,\,i}}$, and $n^{\mathrm{2D}}_{\mathrm{e,i}}(b_i) = 0$ otherwise. The DM in equation (23) is computed along the straight-line ray-path up to $z_s = 3$. We comment that each light ray passes through a sufficient number of gas spheres. For instance, in TNG300-1, there are 1.0×10^4, 2.2×10^4, and 3.7×10^4 gas spheres intersecting a single light ray up to $z_s = 0.4$, 1, and 2, respectively. For TNG300-2 (-3), this number simply decreases by a factor of 2(4). If the number of intersecting gas spheres follows a Poisson distribution, the accuracy of the DM in equation (23) is roughly given by (the number)$^{-1/2}$.

We homogeneously emitted 5400^2 rays through the $6 \times 6\,\mathrm{deg}^2$ field and computed their DMs using equation (23). The resulting angular resolution is 4 arcsec ($= 6\,\mathrm{deg}/5400$). We stored the DM data up to $z_s = 3$ at every $\Delta z_s = 0.02$ step. To see the statistical variation among the maps, we prepared 10 such maps[14] by recycling the same simulation data. Here, the recycling procedure is as follows: (i) swap the coordinates (e.g. $x \leftrightarrow y$) for all particles in the box, (ii) shift the coordinates (e.g. $x \rightarrow x + x_0$ with an arbitrary constant x_0 where the coordinate origin can be freely chosen under the periodic boundary conditions) for all particles, and (iii) finally place these boxes as in Fig. 5 and perform the same ray-tracing calculation. The swapped coordinates (i) and the coordinate shift (ii) were randomly chosen for each map. We prepared the 10 maps for each of the three resolution runs. We checked that the observer does not belong to any halo (the TNG also provides halo catalogues containing halo positions and radii), and thus, the measured DM does not contain the observer's halo contribution.

Fig. 6 is a contour map of the DM from TNG300-1 at $z_s = 1$. This is one of the 10 maps. The red (blue) regions correspond to foreground clusters or galaxies (voids). We present an analysis of the 10 maps in the following section.

5 RESULTS

This section presents measurements of the DM statistics from the mock maps: the mean and variance (subsection 5.1), probability distribution of the DM (subsection 5.2), probability distribution of z_s for a given DM (subsection 5.3), angular power spectrum (subsection 5.4) and angular correlation function (subsection 5.5). Comparisons with the analytical results using the fitting functions (given in Section 3) are also presented.

[14]This number 10 is limited by our hard-disc storage, but sufficient for our studies.

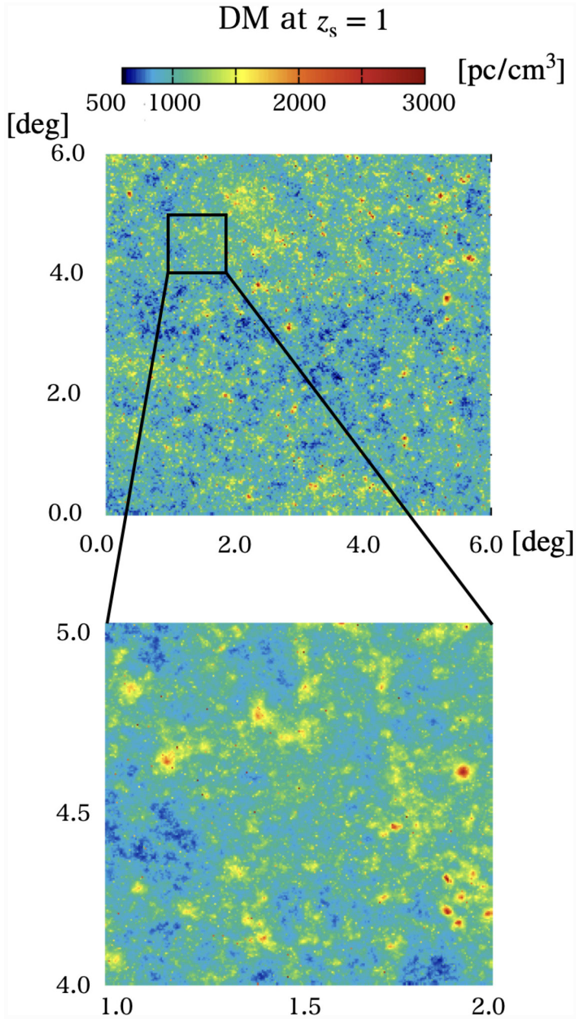

Figure 6. Contour plot of the DM at source redshift $z_s = 1$. The field of view is $6 \times 6\,\mathrm{deg}^2$. The bottom panel is a zoom-in map of $1 \times 1\,\mathrm{deg}^2$. In this and the following figures, DM refers to the cosmological DM (excluding the Milky Way and host-galaxy contributions).

5.1 Mean and variance of the DM

We measured the mean and variance of the DM from the 10 mock maps. As there are 5400^2 data points in each map, the total number of rays ($=10 \times 5400^2 \simeq 2.9 \times 10^8$) is sufficient for statistical analysis. Fig. 7 plots the mean with the standard deviation as a

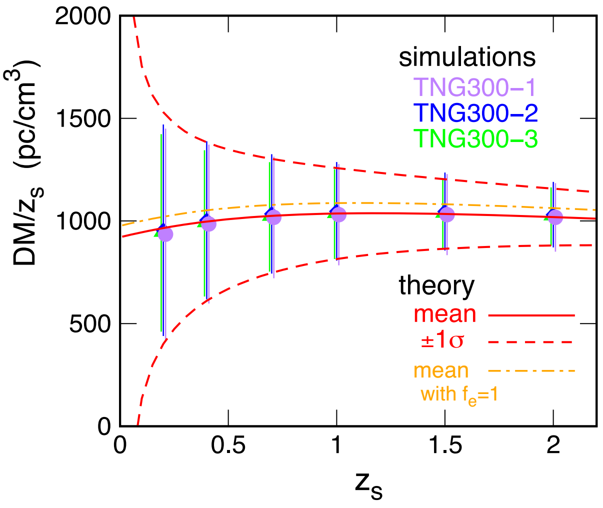

Figure 7. Mean with 1σ standard deviation of the DM as a function of source redshift z_s. The purple, blue, and green symbols are the simulation results measured from the 10 mock maps (one of them is plotted in Fig. 6). The solid (dashed) red curve denotes the analytical predictions for the mean (standard deviation) discussed in Section 2. The dash–dotted orange curve is the same as the solid one, but assuming $f_e = 1$. In this and following figures, the theory refers to the analytical model (in Section 2) using the fitting formulas for $f_e(z)$ and $P_e(k; z)$ (in Section 3).

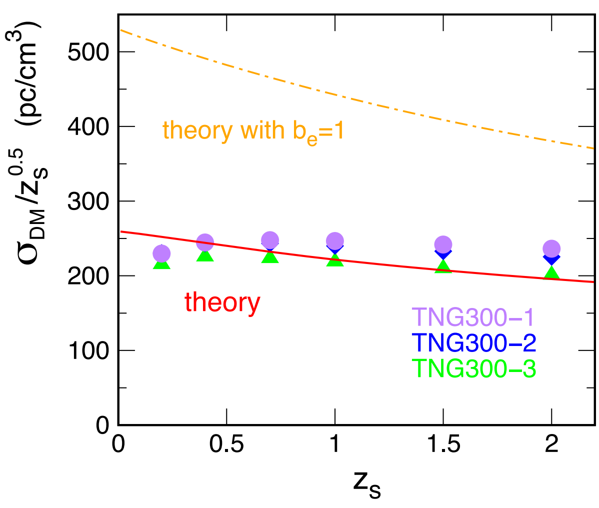

Figure 8. Standard deviation of the DM as a function of z_s. The purple, blue, and green symbols are the TNG300-1, -2, and -3 results. The solid red curve denotes the analytical prediction given in equation (16). The dash–dotted orange curve is the same as the solid one, but assuming that the free electrons exactly trace the dark matter (i.e. $b_e = 1$).

function of z_s. The simulation results are measured at several values of z_s (=0.2, 0.4, 0.7, 1, 1.5, and 2). The mean and variance are obtained by using all the rays in the 10 maps. The solid and dashed red curves are the analytical mean and standard deviation given in equations (7) and (16), respectively. Here and hereafter, the fitting formulas for $f_e(z)$ and $P_e(k; z)$ given in Section 3 are used to compute the analytical predictions, and the theory refers to the analytical model (in Section 2) using these fitting formulas. The figure shows that the theory agrees with the simulations very well. The mean DM is approximately proportional to z_s, $\overline{\rm DM}(z_s) \approx 1000 \times z_s\,{\rm pc\,cm^{-3}}$, which is consistent with previous work (e.g. Ioka 2003). The dash–dotted orange curve is the mean DM for the fully ionized case ($f_e = 1$), as assumed in previous studies (Ioka 2003; Inoue 2004). This simple assumption only slightly overestimates the mean by approximately a few per cent in this redshift range.

Fig. 8 is similar to Fig. 7 but plots only the standard deviations. The agreement between the theory and the simulations is within 10–20 per cent. At large z_s ($\gtrsim 1$), the theory gives slightly lower values than the simulations. This is because $P_e(k)$ was fitted up to $k = 10\,h\,{\rm Mpc}^{-1}$, and gas cooling slightly enhances $P_e(k)$ for $k > 10\,h\,{\rm Mpc}^{-1}$ (see Fig. 3), so fluctuations smaller than this fitting range provides additional contributions to $\sigma_{\rm DM}$, especially at high z_s. The TNG300-1 and -2 results almost converge because fluctuations with k = 1–10 $h\,{\rm Mpc}^{-1}$ contribute most to $\sigma_{\rm DM}$ (see also subsection 3.3), and these runs resolve this scale sufficiently. The TNG300-3 results give a slightly smaller result because of the lowest resolution. From this figure, the standard deviation is roughly given by $\sigma_{\rm DM}(z_s) \approx 230 \times z_s^{0.5}\,{\rm pc\,cm^{-3}}$, which is consistent with the halo-model prediction (McQuinn 2014; Macquart et al. 2020, see also Kumar & Linder 2019). The previous ray-tracing simulation (Jaroszynski 2019, see the dashed line in their fig. 1) gave $\sigma_{\rm DM} \simeq$ 200 and 300 ${\rm pc\,cm^{-3}}$ at $z_s = 1$ and 2, respectively, which are also consistent with our results.

Previously, Shirasaki et al. (2017) and Pol et al. (2019) studied the DM statistics using their dark-matter simulations, assuming the free-electron distribution to be the same as the dark matter distribution (i.e. $b_e = 1$). The dash–dotted orange curve in Fig. 8 corresponds to this case. This assumption may overestimate $\sigma_{\rm DM}$ by a factor of 2.

We comment that although the TNG300 simulations do not contain density fluctuations larger than the box size L (= 205 h^{-1} Mpc), this does not affect the results for $\sigma_{\rm DM}$. If we set the large-scale cut-off $P_e(k) = 0$ for $k < 2\pi/L \simeq 0.03\,h\,{\rm Mpc}^{-1}$ in equation (16), the variance $\sigma_{\rm DM}^2$ is underestimated by < 0.5 per cent in the range z_s = 0–2, because $k^2 P_e(k)$ at such a large scale is too small to give a contribution.

5.2 Probability distribution of the DM

Fig. 9 plots the probability distribution function (PDF) of the DM for several source redshifts (z_s = 0.4, 0.7, 1, and 1.5). The coloured histograms correspond to the different TNG resolutions, which are consistent with each other. The PDF is highly skewed, especially at low z_s, owing to the strong non-Gaussianity of the density fluctuations. The red curves are lognormal distributions with the mean and variance given by the DM-map measurements from TNG300-1. At higher z_s, the simulations approach lognormal distributions. This model is roughly consistent with the simulations, but it has broader tails around the peak and is less skewed than the simulations.

Fig. 10 shows a comparison of the PDF with previous fitting formulas. Das & Ostriker (2006) measured the PDF of the projected matter density using dark-matter N-body simulations. Their purpose was to investigate the PDF of the weak-lensing convergence field. They proposed a modified lognormal distribution (given in their equation 11). Dolag et al. (2015) performed cosmological hydrodynamic simulations and measured the PDF. Their formula depends only on z_s (given in their equation 6). Macquart et al. (2020) proposed a skewed Gaussian PDF calibrated by the halo-model prediction (McQuinn 2014). Here, we used their best-fitting model (their equation 4 with $\alpha = \beta = 3$). In Das & Ostriker (2006) and Macquart et al. (2020), the formulas contain free parameters, but they are fully determined by the mean and variance of the DM measured from TNG300-1. The

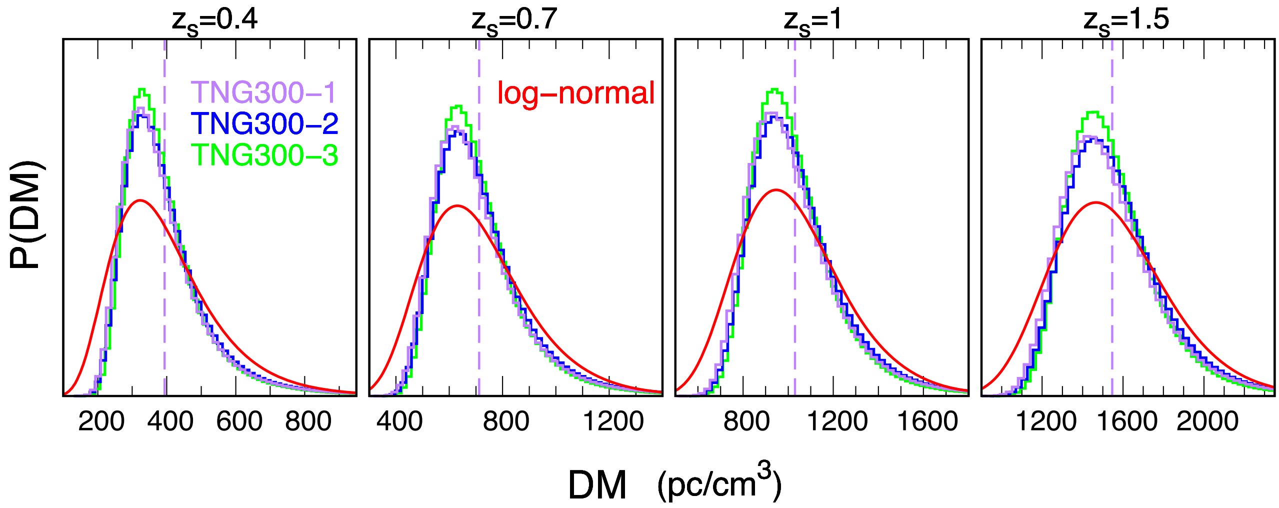

Figure 9. Probability distributions of the DM for several source redshifts z_s, as measured from the mock maps. The purple, blue, and green histograms are the TNG300-1, -2, and -3 results. The vertical dashed line denotes the mean DM measured from TNG300-1. The red curves are lognormal distributions. The vertical axis is in arbitrary units.

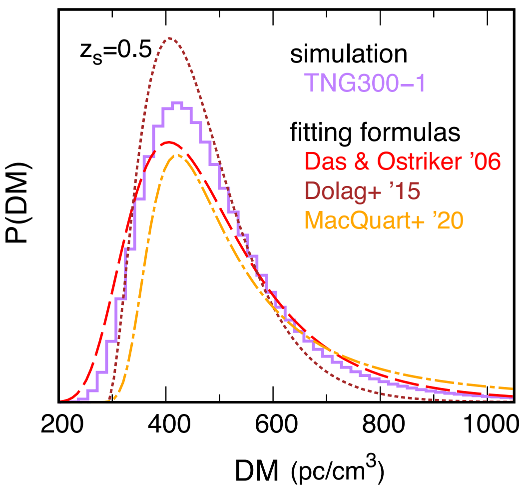

Figure 10. Comparison of probability distributions of the DM at $z_s = 0.5$. The purple histogram is the TNG300-1 result, while the curves denote previous fitting formulas: Das & Ostriker (2006, red-dashed), Dolag et al. (2015, dotted brown), and Macquart et al. (2020, dash–dotted orange) in subsection 5.2.

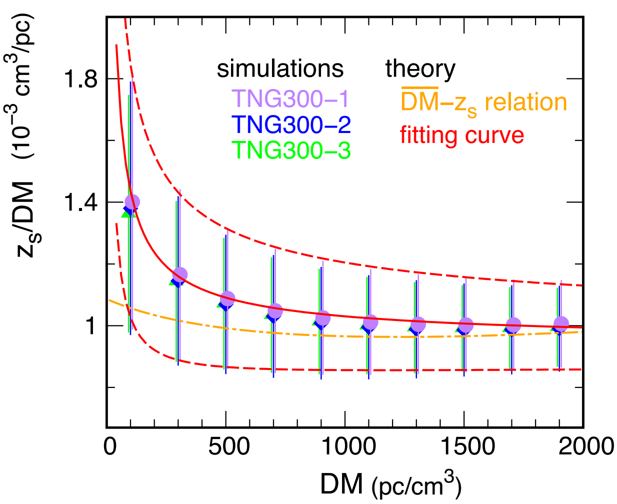

Figure 11. Source redshift inferred from the measured DM. The symbols with 1σ error bars are the simulation results. The dash–dotted orange curve is the analytical $\overline{\mathrm{DM}}$-z_s relation (7). The solid (dashed) red curve is the fit to the mean (1σ error bars), given in equation (25).

figure shows that all the formulas show better agreement with the simulation than the simple lognormal model.

5.3 Probability distribution of the source redshift for a given DM

Since the DM was calculated at every source redshift step $\Delta z_s = 0.02$ up to $z_s = 3$ for each light ray (see Section 4), we can obtain the source redshift z_s corresponding to a given DM. Using all the rays ($=2.9 \times 10^8$), the distribution of z_s for a given DM is also obtained. Fig. 11 plots the mean and 1σ standard deviations for the source redshift z_s inferred from the measured DM. The coloured symbols are the simulation results, while the dash–dotted orange curve is the analytical $\overline{\mathrm{DM}}$–z_s relation (equation 7). As clearly shown in the figure, the $\overline{\mathrm{DM}}$–z_s relation underestimates z_s, especially at low z_s, owing to the highly skewed distribution of the DM (shown in Figs 9 and 10). As the peak of the DM is *lower* than the analytical mean for a given z_s in Fig. 9, the inferred z_s is *higher* than the analytical mean for a given DM. This trend is consistent with a previous finding (Pol et al. 2019, their fig. 3). The figure shows that the standard deviation of z_s is approximately 20 per cent for DM $> 500\,\mathrm{pc\,cm^{-3}}$ but becomes larger for a nearer source. As the statistics of z_s are useful in searching for the host galaxy of an FRB from the measured DM, we fitted the mean $\bar{z}_s$ and standard deviation σ_{z_s} from TNG300-1 in the range DM = 100–2000 $\mathrm{pc\,cm^{-3}}$:

$$\bar{z}_s(\mathrm{DM}) = 0.015\,\mathrm{DM}^{0.26} + 9.4 \times 10^{-4}\,\mathrm{DM},$$
$$\sigma_{z_s}(\mathrm{DM}) = 0.0024\,\mathrm{DM}^{0.61} + 1.2 \times 10^{-5}\,\mathrm{DM}, \qquad (25)$$

where DM is in units of $\mathrm{pc\,cm^{-3}}$. These formulas are plotted as the solid and red-dashed curves in Fig. 11. Though the relation (25) was derived from TNG300-1 for a specific $f_e(z)$ model, it may be used for

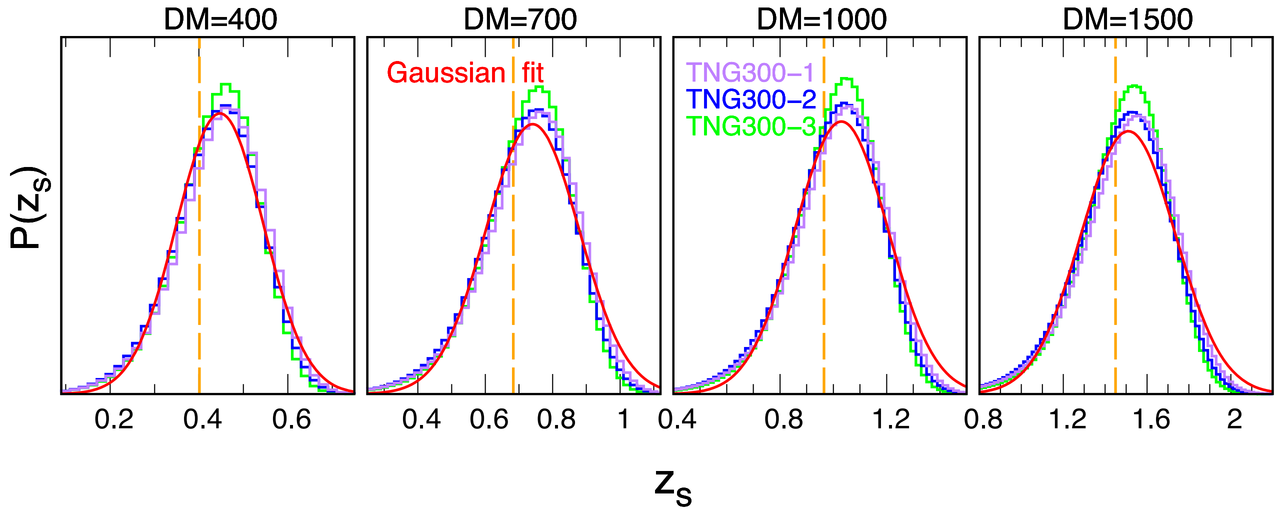

Figure 12. Probability distributions of the source redshift for several given DMs (as denoted over each panel, in units of pc cm^{-3}), as measured from the mock maps. The purple, blue and green histograms are the TNG300-1, -2 and -3 results. The vertical dashed-orange lines are the analytical $\overline{\mathrm{DM}}$–z_s relation (7). The red curves are Gaussian fits with mean and variance given by equation (25). The vertical axis is in arbitrary units.

any $f_e(z)$ model, so long as $f_e(z)$ does not evolve strongly with time (which is valid in our case at $z < 2$, where $f_e \simeq 0.95$, as shown in Fig. 2). In this case, the relation (25) may be used by replacing DM with DM $\times$ $(0.95/f_e)$ for an arbitrary f_e.

Fig. 12 plots the PDFs of the z_s for given DMs. The histograms are the simulation results, while the vertical dashed-orange lines are the values of z_s inferred from the $\overline{\mathrm{DM}}$–z_s relation (7). The analytical expectation of $\bar{z}_s$ is thus systematically lower than the true value by 10–20 per cent, especially for a low DM. The red curves are Gaussian distributions with mean and variance given by equation (25). The PDF of the z_s is well described by a Gaussian.

Walker, Ma & Breton (2020) recently derived a PDF of the z_s by a different approach. Their PDF is based on Bayes' theorem and uses their DM probability distribution and a given FRB redshift distribution. Their PDF (in their Fig. 5) seems consistent with ours, but their result depends on the prior FRB redshift distribution. Hackstein et al. (2020) performed a similar analysis using the same approach.

5.4 Angular power spectrum of the DM

We measured the angular power spectrum of the DM in the same way as discussed for the free-electron power spectrum in subsection 3.3. The Fourier transform of the DM fluctuations in the i-th map (i = 1, 2, ⋯, 10) is denoted as $\widetilde{\delta\mathrm{DM}}_i(\boldsymbol{\ell}; z_s)$ from equation (13). Then the power spectrum for this map is obtained as

$$C_{\ell,i}(z_s) = \frac{1}{N_{\mathrm{mode},\ell}} \sum_{|\boldsymbol{\ell}'|\in\ell} \left|\widetilde{\delta\mathrm{DM}}_i(\boldsymbol{\ell}'; z_s)\right|^2, \quad (26)$$

where the summation is performed in the annulus $\ell - \Delta\ell/2 < |\boldsymbol{\ell}'| < \ell + \Delta\ell/2$, and $N_{\mathrm{mode},\ell}$ is the number of Fourier modes in the annulus with bin-width ($\Delta\log_{10}\ell = 0.1$). We measured $C_{\ell,i}(z_s)$ for the 10 maps to calculate its mean and variance among the maps.

Fig. 13 shows the angular power spectra of the DM at z_s = 0.4 and 1. The symbols with error bars denote the simulation results for the mean and standard deviation among the maps. Here, the minimum multipole is determined by the side length of the map: $\ell_{\min} = 2\pi/(6\,\mathrm{deg}) = 60$. The angular resolution of the maps (= 4 arcsec = 6 deg/5400) is good enough to resolve the signal up to $\ell = 10^4$. If C_ℓ obeys a Gaussian distribution, the error bars scale in proportion to $[(\text{survey area})\Delta\ell]^{-1/2}$, where $\Delta\ell$ is the bin-width. The solid red curves are the theory (15). The red-dashed curves

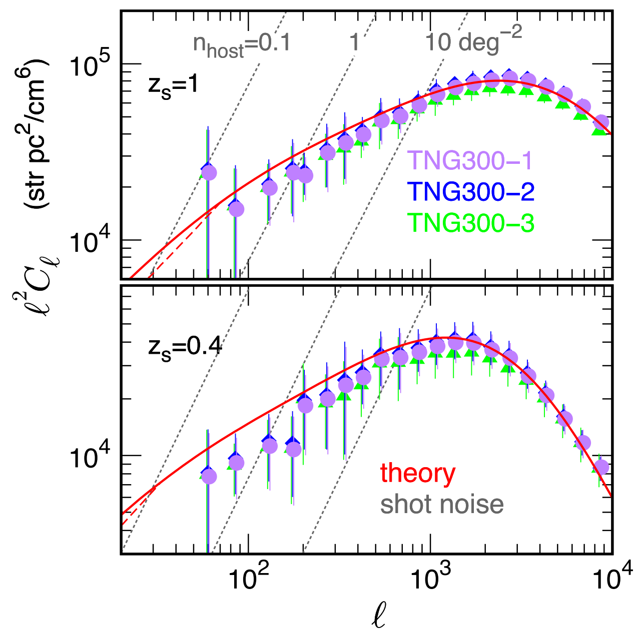

Figure 13. Angular power spectra of the DM at $z_s = 1$ (upper panel) and 0.4 (lower panel). The angular separation θ corresponding to the multipole ℓ is $\theta \sim \pi/\ell = 1\,\mathrm{deg}(\ell/180)^{-1}$. The purple, blue, and green symbols are the TNG300-1, -2, and -3 results, respectively. The mean and 1σ error bars (=standard deviations) are measured from the 10 mock maps. The field of view is $6 \times 6\,\mathrm{deg}^2$, and the error bars scale as $[(\text{survey area})/(36\,\mathrm{deg}^2)]^{-1/2}$. The solid red curves are the analytical predictions (15). The red-dashed curves are the same as the solid ones, but they include the effect of the finite size of the simulation box. The dotted grey lines denote shot noise from the host galaxies ($\sigma^2_{\mathrm{DM,host}}/n_{\mathrm{host}}$) with the intrinsic scatter of $\mathrm{DM_{host}}$, $\sigma_{\mathrm{DM,host}} = 50\,\mathrm{pc\,cm^{-3}}$, and the number densities $n_{\mathrm{host}} = 0.1$, 1, and 10 deg^{-2} from left to right.

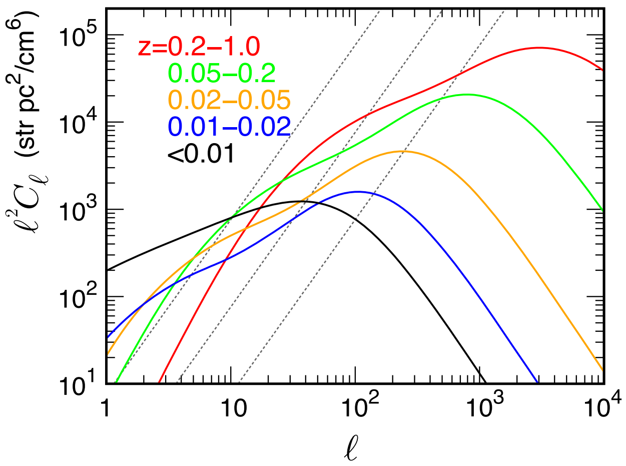

Figure 14. Contribution from different redshifts to the angular power spectrum of the DM. The dotted lines are the same shot noise as in Fig. 13.

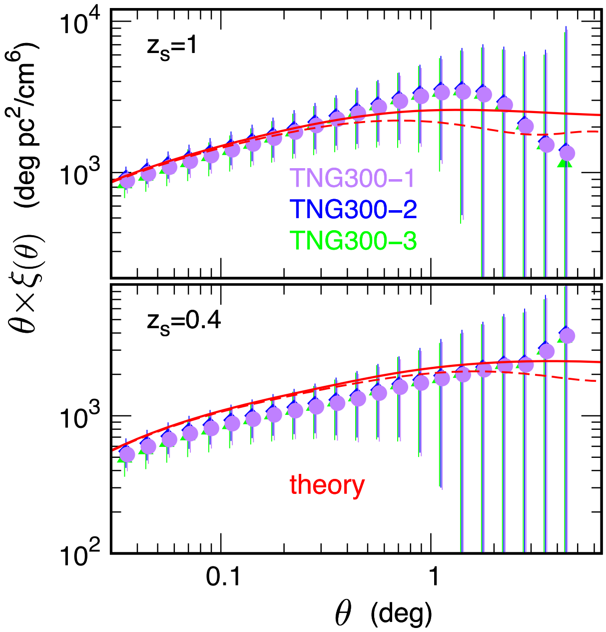

Figure 15. Angular correlation functions of the DM at $z_s = 1$ (upper panel) and 0.4 (lower panel). The purple, blue, and green symbols are the TNG300-1, -2, and -3 results, respectively. The mean and 1σ error bars (=standard deviations) are measured from the 10 mock maps. The field of view is $6 \times 6\,\mathrm{deg}^2$, and the error bars scale as $[(\text{survey area})/(36\,\mathrm{deg}^2)]^{-1/2}$. The solid (dashed) red curves denote the analytical mean from equation (11) (including the finite-simulation-box effect discussed in subsection 5.4).

include the effect of the finite size of the simulation box, where we simply set $P_e(k) = 0$ for $k < 2\pi/L$ in equation (15). This effect only slightly suppresses C_ℓ at large scales ($\ell < 100$). The theory and simulations agree well over a wide range of ℓ, but the simulations are slightly suppressed at small $\ell\,(< 10^3)$. This may be caused by the sample variance of the 10 maps (in other words, 10 maps may not be a sufficient number to measure the mean of C_ℓ precisely). We comment that the power spectra C_ℓ at different $\ell\,(\gtrsim 10^2)$ are correlated due to the non-Gaussian free-electron fluctuations (the non-Gaussian covariance between different ℓ for the weak-lensing power spectrum was discussed in, e.g. Sato et al. 2009). The non-Gaussianity is more important for larger ℓ or lower z_s. The peak of $\ell^2 C_\ell$ in this figure roughly corresponds to the peak of $k^2 P_e(k)$ in Fig. 3 via $\ell_{\rm peak} \simeq k_{\rm peak} r = 2000\,[k_{\rm peak}/(2\,h\,\mathrm{Mpc}^{-1})]\,[r/(1\,h^{-1}\,\mathrm{Gpc})]$ from equation (15).

In actual measurements of C_ℓ, as indicated by several authors (e.g. Shirasaki et al. 2017; Madhavacheril et al. 2019), C_ℓ at small scales is strongly contaminated by shot noise from the host-galaxy contribution, $\mathrm{DM_{host}}$. The shot noise is given by

$$C_{\rm shot} = \frac{\sigma^2_{\rm DM,host}}{n_{\rm host}}, \tag{27}$$

where $\sigma_{\rm DM,\,host}$ is the intrinsic scatter of $\mathrm{DM_{host}}$, and $n_{\rm host}$ is the surface number density per steradian. The shot noise is plotted in Fig. 13 for the cases $\sigma_{\rm DM,host} = 50\,\mathrm{pc\,cm^{-3}}$ and $n_{\rm host} = 0.1$, 1 and $10\,\mathrm{deg}^{-2}$ as illustrative examples. Roughly, the signal must exceed the shot noise in order to be detectable. The figure shows that the small-scale signals are difficult to detect, which is consistent with the previous indication.

Fig. 14 plots the contribution from different redshifts to C_ℓ. At smaller (larger) multipoles ℓ, nearby (distant) structures mainly contribute to C_ℓ because they appear larger (smaller) in the sky. Especially for $\ell < 10$, local structures at $z < 0.01$ (corresponding to $r < 30\,h^{-1}$ Mpc) mainly determine the signal.

We comment that the analytical prediction of C_ℓ is less accurate for very small $\ell\,(< 10)$ because it was derived under the flat-sky approximation. The accuracy of the Limber and flat-sky approximations for projected galaxy clustering and weak-lensing statistics has been discussed in, e.g. Kilbinger et al. (2017) and Fang et al. (2020). Further studies are necessary to estimate the accuracy of these approximations in the DM statistics.

5.5 Angular correlation function of the DM

From equation (10), the correlation function in the i-th map is given by

$$\xi_{\rm i}(\theta; z_s) = \frac{1}{N_{\rm pair}} \sum_{|\boldsymbol{\theta}_1 - \boldsymbol{\theta}_2| \in \theta} \left\{ \mathrm{DM_i}(\boldsymbol{\theta}_1; z_s) - \overline{\mathrm{DM}}(z_s) \right\} \times \left\{ \mathrm{DM_i}(\boldsymbol{\theta}_2; z_s) - \overline{\mathrm{DM}}(z_s) \right\}, \tag{28}$$

where the summation is done in the range $\theta - \Delta\theta/2 < |\boldsymbol{\theta}_1 - \boldsymbol{\theta}_2| < \theta + \Delta\theta/2$, and $N_{\rm pair}$ is the number of DM pairs in the bin-width $\Delta \log_{10}\theta = 0.1$. The mean $\overline{\mathrm{DM}}$ is estimated from the 10 maps. Similarly to C_ℓ, we measured $\xi_{\rm i}(\theta)$ for each of the 10 maps to estimate its mean and variance among the maps. We comment that C_ℓ and $\xi(\theta)$ are not independent but rather are related via the Fourier transform.

Fig. 15 plots the angular correlation functions at $z_s = 0.4$ and 1. The simulation results for the mean and standard deviations are obtained from the 10 maps. The standard deviations increase near the scale of the survey area (=6 deg) because the number of independent DM pairs decreases. The solid red curves are the analytical mean (11). The red-dashed curves include the effect of the finite simulation box, discussed in subsection 5.4. The theory agrees well with the simulations but slightly overestimates them at $\theta \lesssim 1$ deg and $z_s = 0.4$. This discrepancy may be caused by the sample variance. We comment that the simulation results between different values of θ are strongly correlated (see equation 30).

Finally, Fig. 16 plots the analytical correlation functions for a full-sky measurement. This figure shows the analytical results only but covers larger angular scales than Fig. 15. The solid red curves are the theory (11), which are the same as in Fig. 15. Its asymptotic

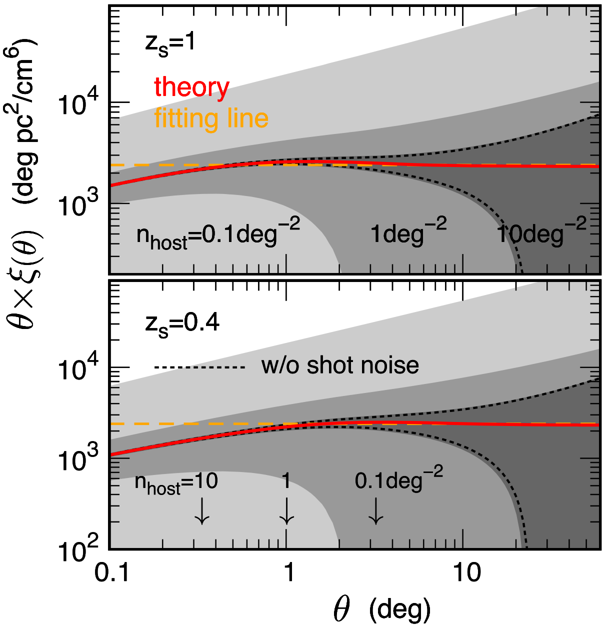

Figure 16. Angular correlation functions of the DM for a full-sky measurement at $z_s = 1$ (upper panel) and 0.4 (lower panel). The solid red curves denote the analytical mean (11). The horizontal orange-dashed lines are the simple fit to the red curves given in equation (29). The shaded area denotes the analytical standard deviation (30) determined by the survey area and the shot noise from the host galaxies, with $\sigma_{\rm DM,host} = 50\,{\rm pc\,cm^{-3}}$ for $n_{\rm host} = 0.1\,{\rm deg^{-2}}$ (light grey), $1\,{\rm deg^{-2}}$ (grey), and $10\,{\rm deg^{-2}}$ (dark grey). The dotted black curves denote the standard deviation without the shot noise (i.e. $n_{\rm host} \to \infty$). The standard deviation simply scales as $[({\rm survey\ area})/(4\pi)]^{-1/2}$. The down arrows in the lower panel denote the average angular separation of the host galaxies (i.e. $n_{\rm host}^{-1/2}$) for $n_{\rm host} = 0.1$, 1 and $10\,{\rm deg^{-2}}$ from right to left.

behaviour at large θ can be described by a simple power law:

$$\xi(\theta; z_s) \approx 2400 \left(\frac{\theta}{\rm deg}\right)^{-1} {\rm pc^2\,cm^{-6}} \quad \text{for } \theta \gtrsim 1\,{\rm deg}. \tag{29}$$

This is plotted by the horizontal orange-dashed lines. We checked that this fit works well at $z_s \gtrsim 0.3$ (i.e. it is insensitive to z_s, because such a large-scale signal is mainly determined by nearby structures, as shown in Fig. 14). Note that equation (29) simply scales as $\propto (f_e/0.95)^2$ for an arbitrary f_e. The grey-shaded regions represent the standard deviation under the assumption of Gaussian density fluctuations (which is valid in the large-scale limit). In this case, the covariance between $\xi(\theta_1; z_s)$ and $\xi(\theta_2; z_s)$ is given by (Joachimi, Schneider & Eifler 2008)

$$\mathrm{Cov}\left[\xi(\theta_1; z_s)\xi(\theta_2; z_s)\right] = \frac{1}{S_W}\int_0^\infty \frac{\ell d\ell}{\pi} J_0(\ell\theta_1) J_0(\ell\theta_2)\left[C_\ell(z_s) + C_{\rm shot}\right]^2, \tag{30}$$

where S_W is the survey area in steradians. The covariance is determined by the survey area at all scales and by the shot noise at small scales. The diagonal element (i.e. $\theta_1 = \theta_2$) corresponds to the variance. In this plot, the shot noise of the host galaxies is considered for the same three cases as in Fig. 13. The dotted black curves denote the standard deviation without the shot noise. This figure suggests that the density $n_{\rm host} = 10\,{\rm deg^{-2}}$ is high enough to neglect the shot noise in the plotted range ($\theta > 0.1$ deg). For $n_{\rm host} = 0.1\,{\rm deg^{-2}}$, the shot noise affects the standard deviation even at very large scales ($\theta \gtrsim 10$ deg). At small scales, non-Gaussian fluctuations become important, and thus, the analytical prediction (30) underestimates the results. On larger scales, the standard deviation increases because there are fewer independent DM pairs in the full sky (i.e. the large-scale signal is limited by the cosmic variance). The down arrows in the lower panel indicate the average angular separation for a given $n_{\rm host}$. Roughly, a signal larger than this scale can be measured. In the near future, when thousands of FRBs are available over the entire sky, we expect the correlation signal at $\theta \gtrsim 3\,{\rm deg}\,(N_{\rm FRB}/4000)^{-1/2}$ to be detected (where $N_{\rm FRB}$ is the number of FRBs and the corresponding number density is $n_{\rm host} \simeq 0.1\,{\rm deg^{-2}}(N_{\rm FRB}/4000)$).

Very recently, Xu & Zhang (2020) reported the first detection of the angular two-point correlation of the DM using 112 FRBs. After subtracting the Milky Way contribution, they measured a statistical quantity – the so-called structure function $D(\theta)$ – which is related to $\xi(\theta)$ as $D(\theta) = {\rm const.} - 2\xi(\theta)$. Their result, plotted in their fig. 3(b), is orders of magnitude larger than our analytical expectation (29), although their error bars are still large. More FRB samples are required to determine whether their signal is of cosmological origin or not.

6 DISCUSSION

6.1 Host-galaxy contribution

So far we have not discussed the host-galaxy contribution because there are two uncertainties in modelling it. First, the host-galaxy properties show significant diversity among the ∼10 currently identified host galaxies (e.g. Tendulkar et al. 2017; Prochaska et al. 2019; Macquart et al. 2020). For instance, the repeating source FRB 121102 is located in a dwarf galaxy, while four other sources identified by ASKAP are in massive galaxies (Chatterjee et al. 2017; Bhandari et al. 2020). The spatial positions of the FRBs in their host galaxies also show variations from the centre to the outskirts. Secondly, the resolution of TNG300 is not fine enough to resolve the inner structure of a host galaxy. These large-box simulations are suitable for studying the cosmological distribution of free electrons, but to study the interiors of galaxies, finer resolution (but smaller box) runs – such as TNG50 and TNG100 – are more suitable. Zhang et al. (2020) and Jaroszynski (2020) recently studied the host-galaxy contribution using TNG100.

When Pol et al. (2019) distributed the sources at a given z_s in their DM simulation, they compared two cases: (i) the sources are distributed randomly, and (ii) its distribution is proportional to the local density contrast. They found that the latter significantly decreased the variance of the cosmological contribution, $\sigma_{\rm DM}^2$. Their results suggest that $\sigma_{\rm DM}$ also depends on host-galaxy properties such as its type (elliptical or spiral), mass, or galaxy bias. More studies are needed on this topic, and we leave this for future work.

6.2 Comparison with other hydrodynamic simulations

Hydrodynamic simulations are the most reliable theoretical tool for studying the free-electron distribution. The cosmological DM has been studied using several simulations, such as Magneticum (Dolag et al. 2015), Illustris (Jaroszynski 2019), and TNG300 (this work). Although these previous results are fairly consistent with ours (see Section 5), a more detailed quantitative comparison among various hydrodynamic simulations is desirable. The free-electron distribution in haloes depends strongly on the stellar and AGN feedback model that expels internal gas to the outside a galaxy.

Lim et al. (2020) recently studied the number density profile of free electrons in haloes with masses of $10^{12-14.5}\,{\rm M_\odot}$ using three hydrodynamic simulations of Illustris, TNG300, and EAGLE (Schaye et al. 2015). These simulations show a discrepancy of ∼ 30 per cent at the halo radius R_{500}, as shown in their figs 5 and 6 (where R_{500} is the radius within which the mean density is 500 times larger than the mean cosmological background density). The discrepancy is larger for a lower mass halo, especially at smaller radius, because such haloes are more sensitive to the feedback model. For instance, Illustris predicts a low inner profile due to strong feedback. In the halo model, $P_{\rm e}(k)$ at small scales ($k \gtrsim 1\,h\,{\rm Mpc}^{-1}$) is determined by the halo mass function and the free-electron density profile in the haloes. Therefore, a similar level of discrepancy is probably present in $P_{\rm e}(k)$.

Because the DM variance is sensitive to $k^2 P_{\rm e}(k)$ around the peak ($k \approx 1$–$10\,h\,{\rm Mpc}^{-1}$), the uncertainty in the feedback model may affect the variance. The angular power spectrum of the DM at small scales ($\ell > 10^3$) is also sensitive to the feedback. However, because its small-scale signal is strongly contaminated by the shot noise (see Fig. 13), the feedback effect will be difficult to observe in C_ℓ.

7 CONCLUSIONS

We have investigated the basic statistics of the cosmological DM using the state-of-the-art hydrodynamic simulations, IllustrisTNG300. Our main purpose is to provide an analytical model for data analysis on the DM statistics.

First, we measured the free-electron fraction $f_{\rm e}(z)$ and its power spectrum $P_{\rm e}(k;\, z)$ from TNG300, which are key ingredients in the DM statistics. It turns out that $P_{\rm e}(k;\, z)$ is consistent with the DMO power spectrum $P_{\rm DMO}(k;\, z)$ at large scales ($k \lesssim 1\,h\,{\rm Mpc}^{-1}$), but it is strongly suppressed at small scales ($k \gtrsim 1\,h\,{\rm Mpc}^{-1}$) owing to stellar and AGN feedback. As a result, the free-electron fluctuations on scales ≈ 1 Mpc contribute most to the DM variance (because $k^2 P_{\rm e}(k;\, z)$ has a peak around that scale). To model $P_{\rm e}(k;\, z)$, we introduced the free-electron bias factor defined by $b_{\rm e}^2(k; z) = P_{\rm e}(k; z)/P_{\rm DMO}(k; z)$. We then provided simple fitting functions calibrated over a wide range of scales and epochs: $f_{\rm e}(z)$ for $z = 0$–8 in equation (17) and $b_{\rm e}(k;\, z)$ for $k < 10\,h\,{\rm Mpc}^{-1}$ and $z = 0$–5 in equation (21). These fitting functions will be useful for future statistical analyses of the free-electron distribution.

Next, we prepared 10 mock sky maps of the DM using the TNG300 data, based on standard ray-tracing techniques. We then measured various DM statistics, such as its mean and variance, PDF of the DM, PDF of the source redshift $z_{\rm s}$ for a given DM, angular power spectrum, and angular correlation function. We calculated the analytical predictions using the fitting formulas for $f_{\rm e}(z)$ and $P_{\rm e}(k;\, z)$ and then validated them against the mock DM measurements. Basic statistics such as the mean, variance, and PDF of the DM were consistent with previous work. The PDF of the DM is highly skewed, while the PDF of the $z_{\rm s}$ is well approximated by a Gaussian. We provided a source redshift–DM relation – $z_{\rm s} = z_{\rm s}({\rm DM})$ in equation (25) – which helps in identifying the host galaxies of FRBs from the measured DMs. The angular correlation function was also computed in subsection 5.5, and we expect it to be detected when thousands of FRBs are available in the coming years.

Throughout this paper, we compared the TNG300 results with three resolution runs to see the numerical convergence. We confirmed that our conclusions do not depend on the resolution, because all the runs resolve the dominant length-scale of the free-electron fluctuations (≈ 1 Mpc) sufficiently. Even so, because the gas distribution in haloes is sensitive to the feedback model, quantitative comparisons with other hydrodynamic simulations are required for further systematic checks. The presented analytical model for the DM statistics will be updated easily by re-calibrating the fitting functions for $f_{\rm e}(z)$ and $P_{\rm e}(k;\, z)$ using more accurate future hydrodynamic simulations.

ACKNOWLEDGEMENTS

We thank the IllustrisTNG team very much for making their simulation data publicly available. We thank Atsushi J. Nishizawa and Shinpei Nishioka for their useful comments. This work is supported by the Ministry of Education, Culture, Sports, Science and Technology (MEXT) and the Japan Society for the Promotion of Science (JSPS) KAKENHI Grant Numbers 20H04723, 17H01131 (RT), 20H01901, 20H01904, 20H00158, 18H01213, 18H01215, 17H06357, 17H06362, and 17H06131 (KI).

DATA AVAILABILITY

The TNG300 simulation data are available at https://www.tng-project.org. The measurement data underlying this article will be shared on reasonable request to the first author.

REFERENCES

Akahori T., Ryu D., Gaensler B. M., 2016, ApJ, 824, 105
Ando R., Nishizawa A. J., Hasegawa K., Shimizu I., Nagamine K., 2019, MNRAS, 484, 5389
Bartelmann M., Schneider P., 2001, Phys. Rep., 340, 291
Bhandari S. et al., 2020, ApJ, 895, L37
Bochenek C. D., McKenna D. L., Belov K. V., Kocz J., Kulkarni S. R., Lamb J., Ravi V., Woody D., 2020, PASP, 132, 034202
Caleb M., Flynn C., Stappers B. W., 2019, MNRAS, 485, 2281
Chatterjee S. et al., 2017, Nature, 541, 58
Chisari N. E. et al., 2019, Open J. Astrophys., 2, 4
Connor L., Lin H.-H., Masui K., Oppermann N., Pen U.-L., Peterson J. B., Roman A., Sievers J., 2016, MNRAS, 460, 1054
Cooke R. J., Pettini M., Steidel C. C., 2018, ApJ, 855, 102
Cooray A., Sheth R., 2002, Phys. Rep., 372, 1
Cordes J. M., Chatterjee S., 2019, ARA&A, 57, 417
Cordes J. M., Lazio T. J. W., 2002, preprint (arXiv:astro-ph/0207156)
Cordes J. M., Wasserman I., 2016, MNRAS, 457, 232
Dai J.-P., Xia J.-Q., 2020, preprint (arXiv:2004.11276)
Das S., Ostriker J. P., 2006, ApJ, 645, 1
Deng W., Zhang B., 2014, ApJ, 783, L35
Dodelson S., 2003, Modern Cosmology. Academic Press, Amsterdam
Dolag K., Gaensler B. M., Beck A. M., Beck M. C., 2015, MNRAS, 451, 4277
Dolag K., Komatsu E., Sunyaev R., 2016, MNRAS, 463, 1797
Fang X., Krause E., Eifler T., MacCrann N., 2020, J. Cosmol. Astropart. Phys., 2020, 010
Fosalba P., Gaztañaga E., Castand er F. J., Manera M., 2008, MNRAS, 391, 435
Fukugita M., Peebles P. J. E., 2004, ApJ, 616, 643
Gao H., Li Z., Zhang B., 2014, ApJ, 788, 189
Hackstein S., Brüggen M., Vazza F., Rodrigues L. F. S., 2020, MNRAS, 498, 4811
Hashimoto T. et al., 2020, MNRAS, 497, 4107
Inoue S., 2004, MNRAS, 348, 999
Ioka K., 2003, ApJ, 598, L79
Ioka K., 2020, ApJ, 904, L15
Ioka K., Zhang B., 2020, ApJ, 893, L26
Jaroszynski M., 2019, MNRAS, 484, 1637
Jaroszynski M., 2020, Acta Astron., 70, 87
Jenkins A. et al., 1998, ApJ, 499, 20
Jing Y. P., 2005, ApJ, 620, 559
Joachimi B., Schneider P., Eifler T., 2008, A&A, 477, 43
Jow D. L., Foreman S., Pen U.-L., Zhu W., 2020, MNRAS, 497, 4956
Kashiyama K., Ioka K., Mészáros P., 2013, ApJ, 776, L39

Keane E. F. et al., 2016, Nature, 530, 453
Kilbinger M. et al., 2017, MNRAS, 472, 2126
Kumar P., Linder E. V., 2019, Phys. Rev. D, 100, 083533
Kumar P., Lu W., Bhattacharya M., 2017, MNRAS, 468, 2726
Lawrence E. et al., 2017, ApJ, 847, 50
Levin Y., Beloborodov A. M., Bransgrove A., 2020, ApJ, 895, L30
Li Z., Gao H., Wei J. J., Yang Y. P., Zhang B., Zhu Z. H., 2020, MNRAS, 496, L28
Liao K., Zhang S. B., Li Z., Gao H., 2020, ApJ, 896, L11
Lim S. H., Barnes D., Vogelsberger M., Mo H. J., Nelson D., Pillepich A., Dolag K., Marinacci F., 2020, MNRAS, preprint (arXiv:2007.11583)
Lorimer D. R., Bailes M., McLaughlin M. A., Narkevic D. J., Crawford F., 2007, Science, 318, 777
Lyubarsky Y., 2020, ApJ, 897, 1
Macquart J. P. et al., 2020, Nature, 581, 391
Madhavacheril M. S., Battaglia N., Smith K. M., Sievers J. L., 2019, Phys. Rev. D, 100, 103532
Marinacci F. et al., 2018, MNRAS, 480, 5113
Masui K. W., Sigurdson K., 2015, Phys. Rev. Lett., 115, 121301
McQuinn M., 2014, ApJ, 780, L33
McQuinn M., 2016, ARA&A, 54, 313
Mead A. J., Peacock J. A., Heymans C., Joudaki S., Heavens A. F., 2015, MNRAS, 454, 1958
Metzger B. D., Berger E., Margalit B., 2017, ApJ, 841, 14
Michilli D. et al., 2018, Nature, 553, 182
Muñoz J. B., Loeb A., 2018, Phys. Rev. D, 98, 103518
Muñoz J. B., Kovetz E. D., Dai L., Kamionkowski M., 2016, Phys. Rev. Lett., 117, 091301
Murase K., Kashiyama K., Mészáros P., 2016, MNRAS, 461, 1498
Naiman J. P. et al., 2018, MNRAS, 477, 1206
Nelson D. et al., 2018, MNRAS, 475, 624
Nelson D. et al., 2019, Comput. Astrophys. Cosmol., 6, 2
Nicastro F. et al., 2018, Nature, 558, 406
Oguri M., 2019, Rep. Prog. Phys., 82, 126901
Petroff E. et al., 2016, Publ. Astron. Soc. Aust., 33, e045
Petroff E., Hessels J. W. T., Lorimer D. R., 2019, A&AR, 27, 4
Pillepich A. et al., 2018a, MNRAS, 473, 4077
Pillepich A. et al., 2018b, MNRAS, 475, 648
Planck Collaboration XIII, 2016, A&A, 594, A13
Planck Collaboration VI, 2020, A&A, 641, A6
Pol N., Lam M. T., McLaughlin M. A., Lazio T. J. W., Cordes J. M., 2019, ApJ, 886, 135
Popov S. B., Postnov K. A., 2010, in Harutyunian H. A., Mickaelian A. M., Terzian Y., eds, Evolution of Cosmic Objects through their Physical Activity. Gitutyun Publ. House NAS RA, Armenia, p. 129
Prochaska J. X. et al., 2019, Science, 366, 231
Rafiei-Ravandi M., Smith K. M., Masui K. W., 2020, Phys. Rev D, 102, 023528
Reischke R., Hagstotz S., Lilow R., 2021, Phys. Rev D, 103, 023517
Sato M., Hamana T., Takahashi R., Takada M., Yoshida N., Matsubara T., Sugiyama N., 2009, ApJ, 701, 945
Schaye J. et al., 2015, MNRAS, 446, 521
Sefusatti E., Crocce M., Scoccimarro R., Couchman H. M. P., 2016, MNRAS, 460, 3624
Shaw L. D., Rudd D. H., Nagai D., 2012, ApJ, 756, 15
Shirasaki M., Kashiyama K., Yoshida N., 2017, Phys. Rev. D, 95, 083012
Shull J. M., Smith B. D., Danforth C. W., 2012, ApJ, 759, 23
Smith R. E. et al., 2003, MNRAS, 341, 1311
Smith R. E., Angulo R. E., 2019, MNRAS, 486, 1448
Somogyi G., Smith R. E., 2010, Phys. Rev. D, 81, 023524
Springel V. et al., 2018, MNRAS, 475, 676
Springel V., 2010, MNRAS, 401, 791
Sunyaev R. A., Zeldovich Y. B., 1970, Ap&SS, 7, 3
Takahashi R., Sato M., Nishimichi T., Taruya A., Oguri M., 2012, ApJ, 761, 152
Tendulkar S. P. et al., 2017, ApJ, 834, L7
Totani T., 2013, PASJ, 65, L12
Villaescusa-Navarro F. et al., 2018, ApJ, 866, 135
Vogelsberger M. et al., 2014, MNRAS, 444, 1518
Walker C. R. H., Ma Y.-Z., Breton R. P., 2020, A&A, 638, A37
Walters A., Ma Y.-Z., Sievers J., Weltman A., 2019, Phys. Rev. D, 100, 103519
Xu S., Zhang B., 2020, ApJ, 898, L48
Zhang G. Q., Yu H., He J. H., Wang F. Y., 2020, ApJ, 900, 170
Zheng Z., Ofek E. O., Kulkarni S. R., Neill J. D., Juric M., 2014, ApJ, 797, 71
Zhou B., Li X., Wang T., Fan Y.-Z., Wei D.-M., 2014, Phys. Rev. D, 89, 107303
Zhu W., Feng L.-L., Zhang F., 2018, ApJ, 865, 147

This paper has been typeset from a TEX/LATEX file prepared by the author.